Thesis for the Degree of Licentiate

# In situ electron microscopy of strain-induced effects on electrical and photovoltaic properties of GaAs nanowires - site specific and quantitative studies

Jonatan Holmér


CHALMERS

Department of Physics
Chalmers University of Technology
Gothenburg, Sweden 2022

In situ electron microscopy of strain-induced effects on electrical and photovoltaic properties of GaAs nanowires - site specific and quantitative studies

Jonatan Holmér



Department of Physics
Chalmers University of Technology
SE-412 96 Gothenburg
Sweden
Telephone +46 (0)31 772 3334

Cover image:
**Upper left:** TEM image of a cross-sectional sample of a GaAs nanowire.
**Lower left:** Single-nanowire I-V characteristics at different strain levels.
**Center:** SEM image of an STM-probe contacting a single nanowire.
**Upper right:** SEM images of a straining series of a GaAs nanowire.
**Lower right:** Single-nanowire short circuit current as a function of strain during different illuminations.

Printed at Chalmers digitaltryck
Gothenburg, Sweden 2022

In situ electron microscopy of strain-induced effects on electrical and photovoltaic properties of GaAs nanowires - site specific and quantitative studies

Jonatan Holmér
Department of Physics
Chalmers University of Technology

# Abstract

Semiconductor nanowires have different physical properties than their bulk counterparts due to their small physical dimensions and high surface-to-volume ratio. The nanowire geometry entails enhanced optical absorption, widened possibilities to grow material heterostructures and ability to withstand high levels of strain. The strain may alter the physical properties further and can be used to tune them. Because of their unique properties, solar cells based on III-V compound nanowires hold promise of becoming both more efficient and less expensive than conventional solar cells. However, nanowire solar cell efficiencies are still far below their theoretical maximum and further optimization is needed. This demands versatile characterization techniques where the microstructure of single nanowires can be related to their properties, and strain-induced effects may be investigated. In this thesis, a nanoprobing in situ electron microscopy technique has been developed to study the electrical and photovoltaic properties of single GaAs nanowires. Furthermore, the quantitative effects of uniaxial strain on these properties were investigated. The results show that the nanowires function as solar cells, with a highest measured single nanowire efficiency of 10.8% during white light emitting diode illumination. Optimization of the electrical contact was found to be crucial for the photovoltaic performance of the wires. Furthermore, tensile strain was shown to increase the photocurrent in the near-infrared spectrum due to a reduction in bandgap energy. These findings provide insights for further optimization of nanowire solar cells.

**Keywords:** Semiconductor nanowires, Solar cells, Elastic strain engineering, In situ electron microscopy

# Acknowledgements

My PhD-studies so far have been a long journey with a lot of ups and downs, and there are several people that have helped me along the way that I would like thank:

First of all, I would like to thank my supervisor Eva for giving me the opportunity to carry out my PhD- studies within her group, for supporting me and believing in me throughout my work. I would like to thank my co-supervisor Lunjie for helping me and teaching me so much and for always being open for discussions that has often lead to new insights and ideas. I would like to thank all the members of Eva Olsson Group, for being great colleagues and creating a nice working atmosphere. A special thanks to my office mate Gustav for all the nice discussions and for helping me out with all kinds of stuff. To Stefan and Ludvig for helping me out with the electron microscopes. To Ola for helping with computer stuff. To all the members of the Materials Microstructure division, for nice lunch discussions. Lastly I would like to thank my friends and family, for being a great support. A special thanks to my partner Linda for always being there for me, and to my son Vincent for forcing me to take my mind of work when I am at home.

# List of appended papers

This thesis is based on the following papers:

**Paper I**
*An STM – SEM setup for characterizing photon and electron induced effects in single photovoltaic nanowires*
Jonatan Holmér, Lunjie Zeng, Thomas Kanne, Peter Krogstrup, Jesper Nygård, Ludvig de Knoop, and Eva Olsson
*Nano Energy 53*, 2018, 175-181

**Paper II**
*Tuning Hole Mobility of Individual p-Doped GaAs Nanowires by Uniaxial Tensile Stress*
Lunjie Zeng, Jonatan Holmér, Rohan Dhall, Christoph Gammer, Andrew M. Minor, and Eva Olsson
*Nano Letters 9*, 2021, 3894-3900

**Paper III**
*Enhancing the NIR photocurrent in single GaAs nanowires with radial p-i-n junctions by uniaxial strain*
Jonatan Holmér, Lunjie Zeng, Thomas Kanne, Peter Krogstrup, Jesper Nygård and Eva Olsson
*Nano Letters 21*, 2021, 9038-9043

# My contributions to the appended papers

Paper I: I developed the experimental technique together with my co-authors. I performed all the in situ STM-SEM experiments and analyzed the data. I wrote the first draft of the manuscript and finalized it together with my co-authors

Paper II: I performed some of the sample preparation using FIBSEM. I was involved in the in situ TEM experimental work. I performed the in situ STM-FIBSEM measurements for the supplementary information. I performed the data analysis of the I-V characteristics.

Paper III: I planned the study and performed all the in situ STM-FIBSEM experiments. I developed the theoretical model used for quantitative analysis of the measured I-V characteristics. I wrote the first draft of the manuscript and finalized it together with my co-authors.

# Contents

# List of Figures

# List of Abbreviations

| | |
|---|---|
| BF | Bright field |
| BSE | Backscattered electron |
| CCD | Charge-coupled device |
| DF | Dark field |
| EBIC | Electron beam induced current |
| ET | Everhart-Thornley |
| FIB-SEM | Focused ion-beam scanning electron microscope |
| GIS | Gas injection system |
| HRTEM | High resolution transmission electron microscopy |
| LED | Light emitting diode |
| MBE | Molecular beam epitaxy |
| NIR | Near-infrared |
| NWA | Nanowire array |
| PCE | Power conversion efficiency |
| SA | Selective-area |
| SC | Self-catalyzed |
| SE | Secondary electron |
| SEM | Scanning electron microscopy |
| STM | Scanning tunneling microscope |
| TCO | Transparent conductive oxide |
| TE | Thermionic emission |
| TEM | Transmission electron microscopy |
| TFE | Thermionic field emission |
| TP | Twin plane |
| WZ | Wurtzite |
| ZB | Zinc Blende |

# 1. Introduction

Semiconductors play a vital role in many of the technologies that our society depends upon, because of their unique physical properties. The possibility to control electrical conductivity and forming electrical barriers makes semiconductors essential for modern electronics, especially as the fundamental component in transistors. Furthermore, their controllable ability to either absorb, propagate or emit light makes them useful for photovoltaic and photonic applications such as solar cells, photodetectors, light emitting diodes (LEDs), lasers and optical fibers. In all these applications, the incorporation of semiconductor nanowires can potentially bring additional capabilities and advantages compared to bulk or thin film semiconductor structures [1].

Nanowires have high aspect ratios and diameters on the nanometer scale. Perhaps the most straight-forward motivation for utilizing semiconductor nanowires is the miniaturization of components, which is essential for a continued technology development. Nanowire-based field effect transistors could provide further downscaling of electronic devices [2]. Nanowires may also be used to miniaturize optical and optoelectronic devices by acting as optical waveguides [3], nanoscale lasers [4] and LEDs [5].

The utility of semiconductor nanowires does not stop at miniaturization though. The greatest potential with semiconductor nanowires stems from the fact that their nanoscale dimensions and high aspect ratio result in unique mechanical, optical and electrical properties. For example, semiconductor nanowires are generally more elastic than their corresponding bulk components, which opens up the possibility to use elastic strain engineering to tune their electrical and optical properties [6]. Strain has been shown to alter both the band structure [7], [8] and the charge transport properties of semiconductor nanowires [9].

One of the most promising applications of semiconductor nanowires is solar cells. The sub-wavelength diameter of the nanowires enable them to act as antennas for incoming sunlight, enhancing the light absorbtion. Furthermore, their high surface-to-volume ratio enable growth of defect-free III-V compound nanowires with direct band gaps on inexpensive substrates such as Si, which is not possible with bulk structures. These and other unique properties make semiconductor nanowires potential building blocks for highly efficient, low-cost solar cells. Tremendous progress have been made in the nanowire solar cell technology during the last two decades, however their efficiencies, with a record at 17.8% [10], are still far from the theoretical limit. For further development, versatile characterization techniques are needed, with the possibility to investigate elastic strain as a means to enhance the nanowire photovoltaic performance, which at present is not widely explored.

The aim of this thesis is to provide insights on how to further optimize nanowire solar cells, with emphasis on the elastic strain engineering route towards higher efficiencies. By the means of in situ electron microscopy, a technique has been es-

tablished for making stable, high-quality electrical contacts to individual nanowires standing vertically on a growth substrate. This enables current-voltage (I-V) measurements during both illuminated and dark conditions, as well as electron beam induced current (EBIC) maps to be recorded. The experimental setup furthermore allows elastic strain to be applied to the nanowires. The technique was used to investigate the electrical and photovoltaic properties, and the effect of strain on those properties, of single p-doped or radially p-i-n doped GaAs nanowires.

# 2. III-V semiconductor nanowires

III-V semiconductors are composed of one element from group III in the periodic table and one from group V. Some examples are GaAs, GaN and InAs. Most III-V semiconductors have direct bandgaps [11], leading to efficient light absorption. They also have high carrier mobilities. III-V nanowires exhibit these properties and additional advantages related to the nanowire geometry, making them the most promising alternative for nanowire solar cells.

## 2.1 Fabrication methods

A prerequisite for all the nanowire-based research and technology is the ability to fabricate high-quality nanowires. In 1964, the growth of Si nanowiskers through a vapor-liquid-solid process was first reported [12]. The first III-V compound nanowires were made in 1997 [13]. Since then, a rapid development has taken place in this field. Today, III-V compound nanowires of high quality and uniformity regarding diameter and length, crystallinity and doping profile can be routinely fabricated.

One way to categorize the different nanowire fabrication methods is to divide them into top-down and bottom-up processes. In a top-down process, the wanted nanostructure is formed by removing material from a bulk sample. This is typically done by forming a protective mask on top of a substrate using lithography, followed by an etching process where the nanowires are formed with the mask as template. It has been demonstrated that III-V nanowire with a wide range of diameter and length can be fabricated using this technique [14]. Even tapered nanowires can be produced this way [15]. However, the most common way to fabricate III-V nanowires today is through bottom-up growth, typically on a substrate. With the bottom-up approach, one can better utilize the unique advantages with nanowires. One advantage is reduced material consumption, as opposed to the top-down approach which inevitably entails a waste of material. Other advantages are the possibilities to form novel, defect-free heterostructures and radial doping profiles, while maintaining control of the nanowire length and diameter. Three main methods are used to grow III-V nanowires, metal-seeded, self-catalyzed (SC) and selective-area (SA) growth [16]. In metal-seeded growth, a metal (usually Au) seed particle is liquefied and forms a eutectic alloy with the group III element, which act as a catalytic for the nanowire growth. The III and V compounds are injected in the gas phase and nucleate at the liquid-solid interface between the catalytic droplet and the substrate. In this way, the nanowire is grown epitaxially in one direction, one atomic layer at the time [17]. One concern with this method is that part of the metal seed particle may be incorporated into the nanowire and degrade the electronic properties [18] [19]. This risk is eliminated in SC growth, where the growth process is similar but the catalyst is a pure group III-element droplet [20]. In SA growth, the substrate is covered

with a mask with defined holes where the nanowire growth take place. The growth mechanism relies on the formation low-index facets of the nanowires controlled by the growth conditions, and no catalyst is needed [21].

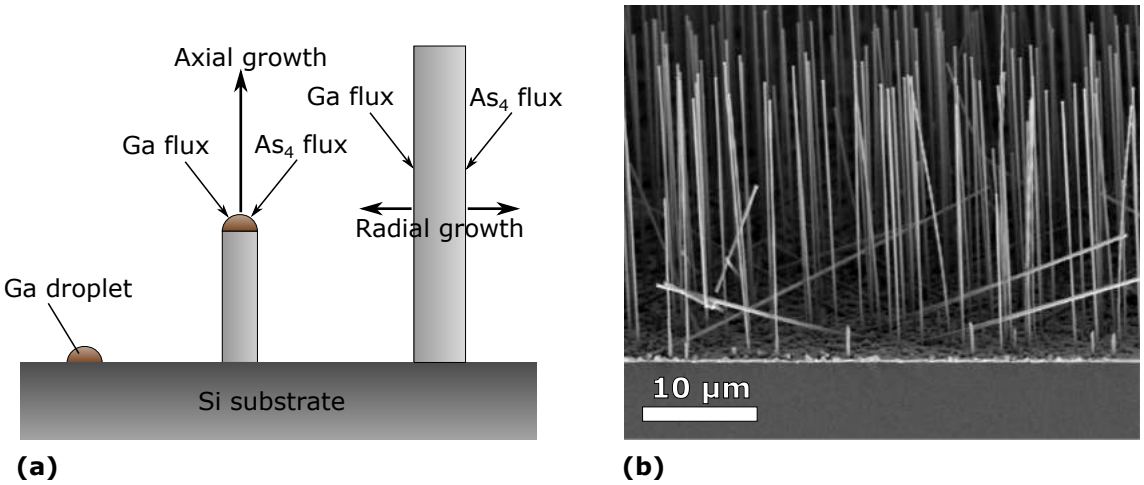


**Figure 2.1:** Schematic illustration **(a)** and SEM image **(b)** of GaAs nanowires grown by self-catalyzed molecular beam epitaxy.

The nanowires used in this work were fabricated through SC molecular beam epitaxy (MBE), see Figure 2.1. In MBE, a substrate is placed in a growth chamber with a pressure of a few $10^{-11}$ Torr. This ultra-high vacuum is needed to avoid unintentional impurities and surface contamination of the grown structure. The substrate is heated to a temperature of several hundreds of °C. Atomic or molecular beams of the growth species are injected into the chamber and adsorb on the substrate. No interaction between the species of different beams occur until they reach the substrate, and this enables fabrication of structures with very abrupt changes in composition or doping [22]. For growth of GaAs nanowires on a Si substrate, a flux of Ga and $As_4$ or $As_2$ is added into the chamber. Ga atoms accumulate at naturally occurring pin-holes in the native $SiO_2$ layer that cover the substrate and form liquid droplets, which eventually become supersaturated and epitaxial growth is initiated at the liquid-solid interface between the droplets and the substrate [23]. Since it is the structure of the native oxide that determines where growth will be initiated, the positions of the nanowires will be random and some will grow at an angle <90 degrees to the substrate due to the formation of polycrystalline seeds [24]. However, it is possible to grow a thicker $SiO_2$ layer ($\sim$20 nm) and create holes in it with lithography, when control of the growth positions of the nanowires is needed. By optimizing the ratio between the diameter and thickness of the holes in the oxide, a high yield of ordered arrays of vertical nanowires can be achieved [25][26]. When the desired length of the nanowires has been achieved, the Ga droplet can be consumed and the growth conditions such as temperature and beam fluxes may be changed to promote radial growth, in order to increase the diameter or form radial doping structures. Doping can be incorporated both during axial and radial growth by adding a flux of the dopant element [27].

## 2.2 Microstructure and properties

III-V nanowires generally have high crystal quality, with a low density of impurities, point defects and dislocations. However, issues regarding surface defects, stacking faults due to polytypism and twin boundaries are common. The surface of the nanowire constitute a disruption in the periodic crystal lattice which may affect the electronic properties. Especially, electronic states introduced by dangling bonds at the surface may act as recombination centers for charge carriers, an effect that can severely impair the performance of nanowire photovoltaic devices. Surface passivation may be used to mitigate these effects [28]. III-V nanowires that have been exposed to air are typically oxidized and covered with a thin native oxide layer. This may obstruct the formation of low-resistive electrical contacts to the nanowires by forming an insulating barrier.

Regarding the crystal structure of III-V semiconductors, either the cubic zinc-blende (ZB) or the hexagonal wurtzite (WZ) structure is thermodynamically stable in bulk form, depending on the ionicity of the compound [29]. The ZB structure can be described as having a stacking sequence of ABCABC... and WZ ABABAB... along the [111] direction, where each A, B or C represents a bilayer consisting of both a layer of III-type atoms and a layer of V-type atoms, see Figure 2.2. In the nanowire geometry, even the structure that is not stable in bulk form can be found for most of the III-V materials. For example, the WZ structure is not stable in bulk GaAs, but can exist in GaAs nanowires. Even a mixture of the two phases within the same nanowire is possible, a phenomenon known as polytypism and illustrated in 2.2 (a) [30]. By varying the growth conditions, the switching between WZ and ZB structure could be controlled within the nanowire [31]. Since the crystal structure affect the band structure of the material this could for example be utilized to form quantum dots [32]. However, unwanted polytypism may constitute a problem in other applications. For example, theoretical studies have shown that segments of WZ structure in otherwise ZB GaAs nanowires can reduce the conductance significantly [33].

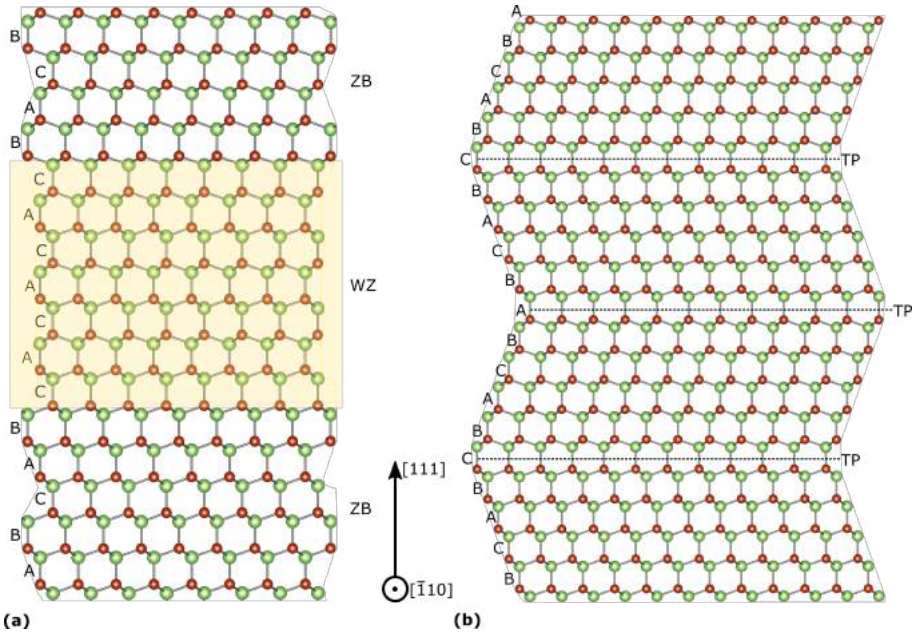


**Figure 2.2:** Schematic structure of **(a)** mixed ZB and WZ crystal phases and **(b)** twin planes in III-V nanowires.

Another phenomenon that is common in ZB III-V nanowires is the formation of twin planes (TP). A TP arises when the crystal orientation is rotated 60° along the [111] axis, see Figure 2.2 (b), and this can occur spontaneously during bottom-up growth of GaAs nanowires. A high density of TPs in the ZB structure may reduce the electron and hole mobilities [33]. However, if the average distance between TPs is >25 nm, the effect on the electron mobility is insignificant [34]

## 2.3 Strain engineering

When a crystal is exposed to external stress, it is either plastically deformed or elastically strained before fracture. Plastic deformation is irreversible and imply introduction of crystallographic defects which normally lead to degradation of desirable electronic properties in semiconductors [35]. Elastic strain on the other hand is a reversible process where the distance between the atoms in the crystal changes as a function of applied stress. Since the atomic positions in a periodic crystal affects the band structure, elastic strain may lead to enhancements of the electrical and optical properties of the crystal [6]. As an example, strain engineering is commonly used in complementary metal organic semiconductor (CMOS) technology, where strained Si is used to enhance charge carrier mobilities [36].

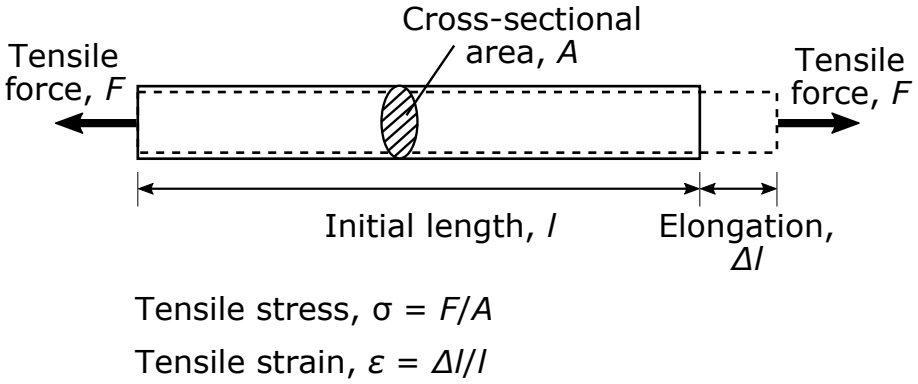


**Figure 2.3:** Definitions of tensile stress and strain.

Tensile strain is defined as the ratio between the elongation due to stress and the original length of an object [37], see Figure 2.3 for further details. Conventional materials can generally only withstand strain levels <0.2% before plastic deformation or fracture occurs [38]. For thin films grown on lattice mismatched substrates, generally only up to 1% strain can be achieved without introducing defects [39]. In contrast, semiconductor nanowires can withstand strain levels significantly higher than their bulk counterparts, even as high as 10% in the case of Si nanowires [40]. This opens up the possibility to use elastic strain to tune the properties over a much wider range than what is possible in bulk structures. Extensive research has been carried out to investigate the impact of strain on III-V nanowires. For example, uniaxial strain has been shown to alter the electron transport properties and the energy of surface states in InAs nanowires [41], [42]. Moreover, strain induced by bending have been shown to affect the effective mass of valence electrons in GaAs nanowires [43]. In Paper II we investigated the effect of uniaxial tensile strain on the electron hole mobility in GaAs nanowires. There are many reports on strain-induced band gap modifications in GaAs nanowires. For example, mechanically induced uniaxial tensile strain in ZB GaAs nanowires has been shown to reduce the band gap energy with up to 296 meV [8]. Furthermore, strain induced by highly lattice mismatched core-shell structures in GaAs nanowires could reduce the band gap by 40% [44]. Such large modifications of the band gap may be of high interest for many applications, especially solar cells, which is discussed in Chapter 3.

# 3. Nanowire solar cells

In order to understand the potential of using nanowires in solar cells, it is necessary to have an understanding of the principles of conventional solar cells. This chapter therefore starts with some basic theory of solar cells, then continues to the design and advantages of nanowire solar cells. Lastly, different techniques for characterizing nanowire solar cells are discussed.

A solar cell is a device capable of converting solar energy into electrical energy. Figure 3.1 shows the general design of a conventional solar cell. The active part is composed of a semiconductor doped to form a p-n junction. Here, the sunlight is absorbed by the semiconductor, and in this process electron-hole pairs are created. These mobile charges are subsequently separated by a built-in electric field that arises at the junction. Electrons go into the n-doped part and holes go into the p-doped part. If the p- and n-doped regions are electrically connected by an external circuit, a current will flow in order to equalize the potential of the two regions. This current is called photocurrent, $I_{ph}$, and can be used to power an electrical device, or charge a battery for example.

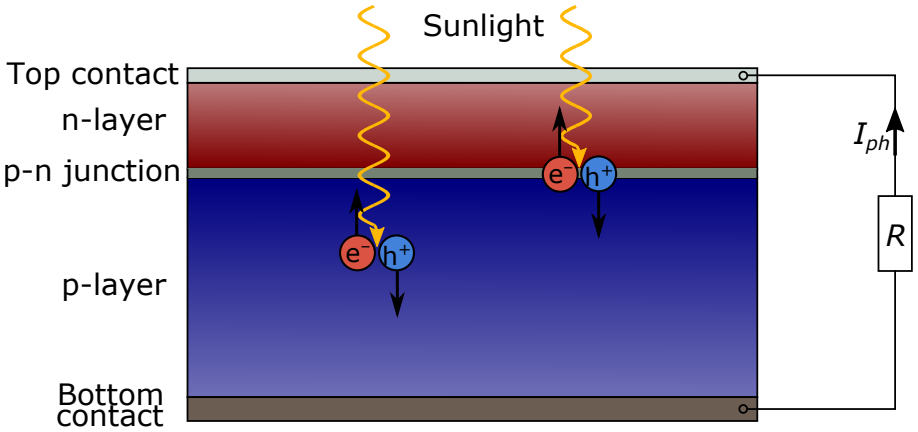


**Figure 3.1:** Schematic structure of a conventional solar cell. The built-in field at the p-n junction separates the charge carriers generated by absorption of sunlight, giving rise to a photocurrent.

## 3.1 The p-n junction

Evidently, the p-n junction plays a key role in the function of a conventional solar cell. Without it, there would be no separating mechanism for the generated electron-hole pairs, and no electrical current would be generated by the cell. To a large extent, it is the physical properties of the p-n junction that governs the function of a conventional solar cell, and the details of those properties will be discussed in this section.

In an intrinsic semiconductor, the Fermi energy ($E_F$) is in the middle of the gap between the conduction band and the valence band, but it can be shifted by doping the semiconductor. In an n-doped semiconductor there is an excess of free electrons in the conduction band, and $E_F$ is shifted upwards, see Figure 3.2 (a). In a p-doped semiconductor there is an excess of free holes in the valence band, and $E_F$ is shifted downwards, see Figure 3.2 (b).

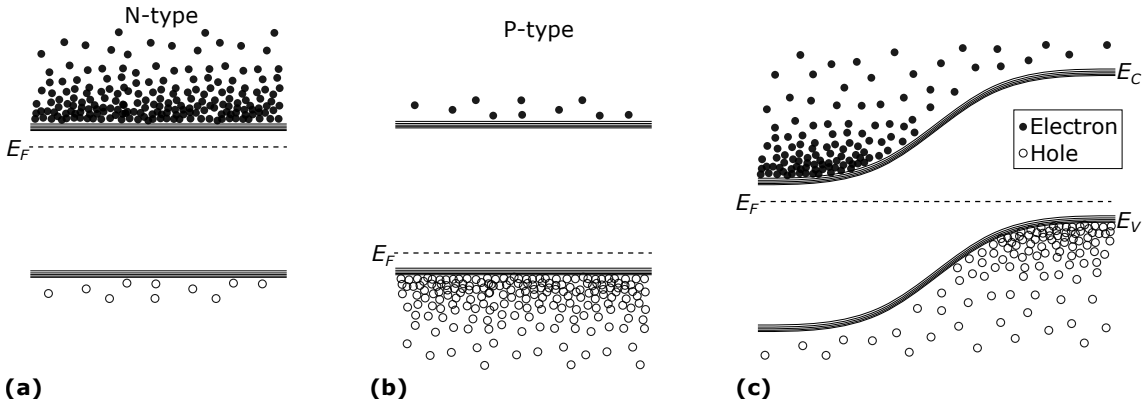


**Figure 3.2:** **(a)** Band diagram of a n-doped semiconductor. The Fermi energy is closer to the conduction band than the valence band. **(b)** Band diagram of a p-doped semiconductor. The Fermi energy is closer to the valence band than the conduction band. **(c)** Band diagram of a p-n junction in equilibrium. The Fermi-levels are aligned which results in a slope in the conduction and the valence band.

If the n-doped and p-doped regions of the semiconductor are brought into physical contact, the Fermi-levels will become aligned throughout the whole material when equilibrium is reached [45]. Still, deep into the n-doped (p-doped) region $E_F$ will remain close to the conduction (valence) band. As a result, there will be a slope in the energy of the conduction and valence band in the region at the p-n junction, see Figure 3.2 (c), meaning that there is an electric field across this region. The physical origin of this field can be explained through the following reasoning: The n-doped region has an excess of free electrons and the p-doped region has an excess of holes. When they are brought into contact there will accordingly be a diffusion force on the electrons towards the p-doped region and a diffusion force on the holes towards the n-doped region. When the electrons diffuse to the p-side, they will recombine with the holes there and leave behind uncompensated positive charges in the form of immobile donor ions, see Figure 3.3 (a). Analogously, the holes diffusing over to the n-side will leave behind a negative charges. These growing charges will give rise to an electric field that counteract the diffusion force on the charge carriers. When equilibrium is reached the diffusion force and the electric field force will completely cancel each other out. The region where the field is present is called the depletion layer, because the free charge carriers are almost depleted here [46].

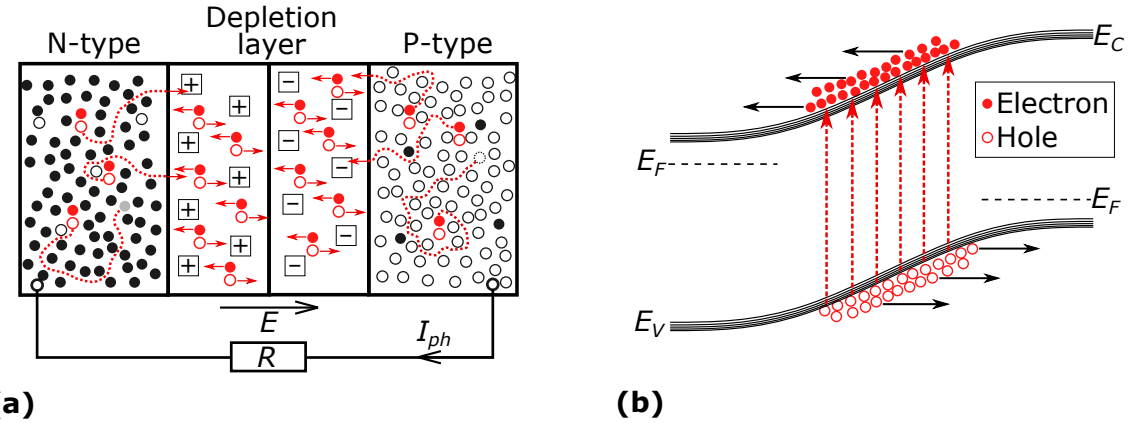


**Figure 3.3:** **(a)** Cross section of a p-n junction under illumination. The field across the depletion layer arises due to uncompensated ion charges. Charge carriers generated in the depletion layer are separated directly by the built-in field. Charge carriers generated in the neutral regions need to diffuse to the depletion layer to get separated, and may recombine before they get there. **(b)** Band diagram of a p-n junction under illumination. The generated electrons and holes are separated by the built-in field. This results in a difference in Fermi energies between the n-side and the p-side, and gives rise to a photocurrent.

When the p-n junction is illuminated by light, the photons could be absorbed and electron-hole pairs created. The field across the junction will act as a separator, forcing the electrons to move into the n-doped region and the holes to move into the p-doped region, illustrated in Figure 3.3 (a) and (b). The concentration of electrons in the n-doped region and the concentration of holes in the p-doped region will then be higher than the equilibrium case. This will split the Fermi-levels of the two regions, and be a driving force for the electrons to go to the p-side and holes to go to the n-side through the external circuit [46], giving rise to a net photocurrent. Not all photons will be absorbed inside the depletion layer though. Some of them will be absorbed some distance away from the junction, either in the n-doped or the p-doped region. The generated minority carriers (electrons in the p-type region and holes in the n-type region) first need to diffuse to the junction in order for the built-in field to force them into the opposite region, see Figure 3.3 (a). While they are diffusing, there is a probability that they recombine, meaning that an electron in the conduction band fills a hole in the valence band. The charge carriers that recombine before reaching the junction will not contribute to the photocurrent. Recombination is discussed in further detail in section 3.3.

The built-in field of a p-n junction acts as a barrier for majority carriers (holes in the p-type region and electrons in the n-type region). If an external electrical bias is applied, this barrier can be either increased or decreased, depending on the polarity. In the so called forward bias condition, with the positive pole connected to the p-side, the barrier is lowered and the majority carriers can pass the junction into the opposite region, see Figure 3.4 (a). Since the concentration of majority carriers is high in a doped semiconductor, the current in the forward bias regime can become large. The energy distribution of the majority carriers can be approximated with a Maxwell-Boltzmann distribution. As the voltage is increased and the barrier

is reduced more and more, the number of electrons and holes that can pass the depletion layer will therefore increase exponentially, and the forward bias current will have an exponential voltage dependence [45].

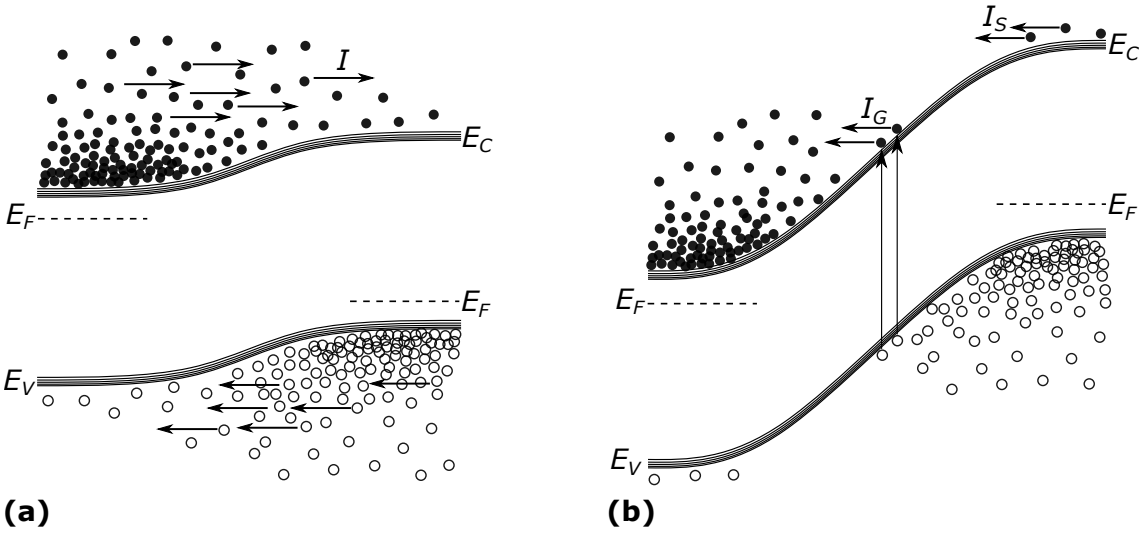


**Figure 3.4:** **(a)** Band energy diagram of a forward biased p-n junction. The Fermi levels of the p- respectively the n-side are split up, causing the energy barrier to decrease. **(b)** Band energy diagram of a reverse biased p-n junction. The Fermi levels of the p- respectively the n-side are again split up, but in the other direction compared to forward bias, causing the energy barrier to increase.

In the reverse bias condition though, the barrier is increased as a result of the additional voltage drop over the junction, see Figure 3.4 (b). In this situation, there are two types of currents that can flow, the generation current $I_G$ and the saturation current $I_S$. $I_G$ is caused by the thermal generation of charge carriers in the depletion layer, which will be separated by the field at the junction. $I_S$ is constituted of minority carriers that passes the junction, i.e. electrons that are swept by the field from the p-side to the n-side, and holes that are swept in the other direction. Since the concentration of minority carriers is usually very small compared to majority charge carriers in a doped semiconductor, $I_S$ will take small values. As the reverse bias increases, the field strength across the junction will increase, but the concentration of minority carriers will remain the same. $I_S$ will therefore be independent of the applied voltage, hence the name saturation current [45].

Both $I_G$ and $I_S$ are usually assumed to be negligibly small, and in that case the p-n junction is current rectifying, meaning a current can only flow in one direction. The current through a p-n junction as a function of applied bias, $I(V)$, can be modeled by the Shockley equation:

$$I = I_S \left[ \exp\left( \frac{qV}{nk_BT} \right) - 1 \right]. \tag{3.1}$$

Here $q$ is the elementary charge, $k_B$ is the Boltzmann constant, $T$ is the absolute temperature, and $n$ is the so called ideality factor of the junction. This equation

clearly fulfills the requirement that the current should increase exponentially at positive bias and quickly stabilize at $I_S$ at negative bias. $I_G$ is not taken into account in this model. Furthermore, $I_S$ can be related to the band gap energy ($E_g$) of the junction through the expression

$$I_s = Ce^{-E_g/nk_BT}, \tag{3.2}$$

where $C$ is a constant related to the semiconductor [47].

## 3.2 Solar cell I-V characteristics

As mentioned earlier, the p-n junction is the basis of a conventional solar cell. Therefore, we can use the Shockley equation as a basis to model the I-V characteristics of a solar cell. However, some additions need to be made to make the model accurate. First of all, in a solar cell device the p-n junction needs to be connected to an external circuit in order to harvest the electrical energy. A finite resistance will always be present in this circuit and especially at the contacts between the circuit and the semiconductor. This resistance will be in series with the p-n junction, and is labeled $R_{se}$ in the model. Furthermore, in practical devices there may exist a current path in parallel with the p-n junction. It can be the result of inhomogeneuos doping or bad insulation between the top and bottom contact. This is included in the model by a so-called shunt resistance $R_{sh}$, in parallel with the junction. Finally, the photocurrent $I_{ph}$ that is generated when the solar cell is illuminated can be represented by a current generator in the model. The direction of this current will be the same as for reverse bias. The equivalent electrical circuit of this model is shown in Figure 3.5 (a). Here the p-n junction is represented by a diode since it is current rectifying. With these additions, equation 3.1 becomes

$$I = \frac{V - R_{se}I}{R_{sh}} + I_S\left[\exp\left(\frac{q(V - R_{se}I)}{nk_BT}\right) - 1\right] - I_{ph}. \tag{3.3}$$

This is known as the single diode model for solar cells [48].

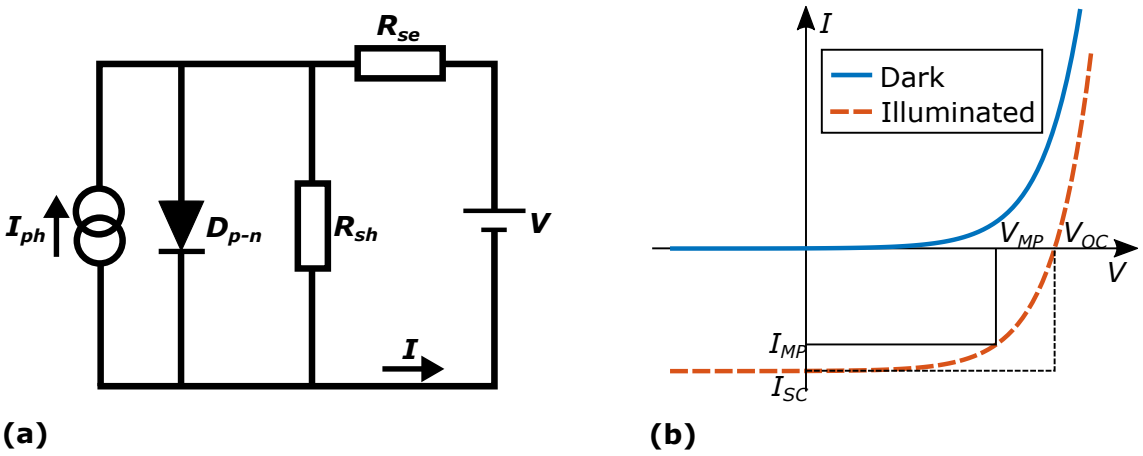


**Figure 3.5:** **(a)** Equivalent circuit of a non-ideal solar cell using the single-diode model. **(b)** I-V characteristics of an ideal solar cell. In the dark state the current is practically zero in the reverse bias regime and has an exponential dependence on the voltage in the forward bias regime. In the illuminated state the I-V curve is a superposition of the dark I-V curve and the photocurrent $I_{ph}$. The important parameters $I_{SC}$ and $V_{OC}$ can be extracted from the illuminated I-V curve.

Figure 3.5 (b) shows the I-V characteristics of an ideal solar cell under dark and illuminated conditions. In this case, the I-V characteristics during illumination follows the superposition principle, which means it is the exact same I-V characteristics as in the dark, only shifted downwards by the absolute value of $I_{ph}$. From the I-V characteristics during illumination it is possible to extract some important parameters that are commonly used to assess the performance of solar cells. The short circuit current $I_{SC}$ and the open circuit voltage $V_{OC}$ are two such parameters. $I_{SC}$ can be found by reading the value of the current where the I-V curve intersects the y-axis, and $V_{OC}$ is the value of the voltage where the I-V curve intersects the x-axis, see Figure 3.5 (b). If the effect of $R_{se}$ and $R_{sh}$ is negligible, then $I_{SC} = I_{ph}$ and equation 3.3 can be used to find an expression between $I_{SC}$ and $V_{OC}$:

$$V_{OC} = \frac{nk_BT}{q} \ln\left(\frac{I_{SC}}{I_S} + 1\right) \tag{3.4}$$

The resistance of the load in the external circuit will determine in which point on the I-V curve the solar cell will operate, i.e what the values of the current and voltage will be. If the solar cell is operated at short circuit conditions, the current will have the highest possible value, $I_{SC}$, but the voltage will be $V = 0$. The power output in this situation will therefore be $P_{Out} = IV = I_{SC} \cdot 0 = 0$. If it is operated at open circuit conditions the voltage will have the highest value, $V_{OC}$, but the current will be zero so again, $P_{Out} = 0$. Somewhere in between these extremes an optimum will exist, generating the highest possible $P_{Out}$. This is the maximum power point $[V_{MP}, I_{MP}]$, indicated in Figure 3.5 (b). The third parameter for assessment, the fill factor $(FF)$, is then defined as

$$FF = \frac{I_{MP}V_{MP}}{I_{SC}V_{OC}} \tag{3.5}$$

Geometrically, $FF$ is the ratio between the area of the solid line rectangle and the dashed line rectangle in Figure 3.5 (b). The fill factor can thus be said to be a measure of the "squareness" of the illuminated I-V curve, and the more square the curve is, the higher is the generated power. Further, the power conversion efficiency (PCE) of a solar cell is defined as

$$PCE = \frac{P_{Out}}{P_{In}} = \frac{FF * I_{SC} * V_{OC}}{P_{In}}. \tag{3.6}$$

$P_{In}$ is the input power coming from the light, which is 100 mW per cm$^2$ for 1 Sun illumination.

## 3.3 Loss mechanisms in solar cells

Real solar cells can never be truly ideal and several mechanisms exists that may introduce losses. First of all, the parasitic resistances $R_{se}$ and $R_{sh}$ may have a detrimental effect on the solar cell performance, see Figure 3.6. A large $R_{se}$ reduces the $FF$. A small $R_{sh}$ reduces both $FF$ and $V_{OC}$, and a combination of both large $R_{se}$ and small $R_{sh}$ additionally reduces $I_{SC}$. All these effects reduces the PCE of the solar cell.

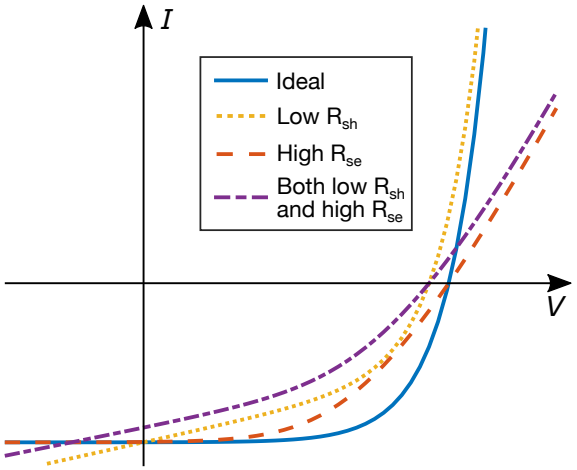


**Figure 3.6:** Illustration of how $R_{se}$ and $R_{sh}$ affects shape of the illuminated I-V curve and the performance of a solar cell.

Another loss mechanism in solar cells is recombination. Electrons and holes generated in a semiconductor have a limited lifetime, and will therefore eventually recombine. There exist different recombination processes, and they can be divided into radiative recombination and non-radiative recombination. In order for a solar cell to achieve the theoretical maximum output voltage, the recombination processes should be strictly radiative. Radiative recombination means that a photon is produced when an electron-hole pair recombines. This photon can then be recycled within the absorbing material to create another electron-hole pair, a process that helps maintaining a high concentration of charges and thus a high voltage difference

between the n- and p-doped regions during illumination. Non-radiative recombination on the other hand only results in loss of available charge carriers and reduces the $V_{OC}$ of the solar cell [49]. Non-radiative recombination can occur when electronic states are introduced within the band gap because of defects in the crystal structure or dangling bonds at the surface of the semiconductor [35]. It is therefore important to have high crystal quality and in some cases surface passivation, in order to reach a high PCE. The recombination processes are taken into account by the ideality factor, $n$, in the single diode model. For the ideal case, with strictly radiative recombination occurring in the neutral regions, $n = 1$. However, for strictly non-radiative recombination occurring in the depletion region of the junction, $n = 2$. A mixture of the two processes results in $1 < n < 2$. If additional junctions are present in the circuit, for example at the contact, it is possible that $n > 2$ [50].

A more fundamental cause of energy loss in solar cells is thermalization. Whenever a photon, with energy higher than $E_g$ of the active material in the solar cell, is absorbed, an electron will be excited to an energy level above the bottom of the conduction band, see Figure 3.7 (a). This excess energy will rapidly be transferred into the semiconductor crystal in the form of lattice vibrations, in a process termed thermalization. Therefore, the maximum energy that can be harvested from an absorbed photon is $E_g$, regardless of the initial photon energy. At this point, it would seem that a larger band gap always results in a higher efficiency, since then a lesser part of the photon energies is lost through thermalization. However, since no photons with energies $< E_g$ can be absorbed, a larger $E_g$ will result in fewer absorbed photons. Therefore, the optimal choice of $E_g$ will be a compromise between minimizing thermalization losses and maximizing absorption, and it will depend on the spectral irradiance of the incoming light. Figure 3.7 (b) shows the AM1.5 standard solar spectrum [51] and the usable intensity for $E_g = 1.7$ eV and $E_g = 1.1$ eV under the assumption that every absorbed photon contributes with an energy equal to $E_g$ and no photons with energies less than $E_g$ get absorbed. It is evident that a high band gap solar cell make better use of the high energetic (short wavelength) photons but cannot use the low-energetic ones at all, while a low band gap solar cell absorb a higher number of photons, but make poor use of the high-energetic ones. The optimal band gap for the AM1.5 spectra must therefore be somewhere between 1.7 and 1.1 eV, more particularly at 1.34 eV. At this band gap, the maximum theoretical efficiency for a p-n junction solar cell that is only limited by radiative recombination is 33.16% [52]. This is the so called detailed balance limit [53], famously known as the Shockley-Queisser limit.

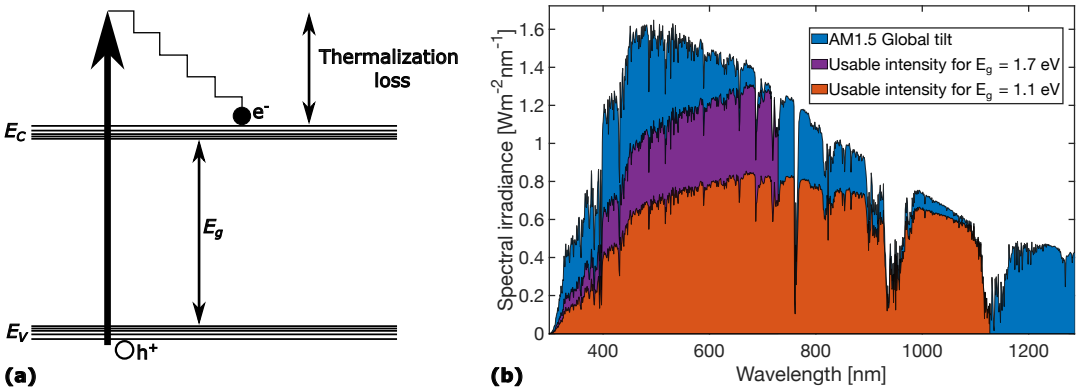


**Figure 3.7:** **(a)** Principle of thermalization. A photon with energy larger than $E_g$ excites an electron to an energy level higher than $E_C$. The excess energy is transferred to the crystal lattice in the form of phonons. **(b)** The AM1.5 solar spectrum and the maximal usable intensity for a single band gap solar cell with $E_g = 1.7$eV and $E_g = 1.1$eV.

In order to overcome the compromise between high absorption and low thermalization losses, materials of different band gaps are stacked upon each other in multijunction solar cells. In this way, the Shockley-Quiesser limit can be beaten and the record efficiency for a multijunction solar cell is 39.5 % [54], which is the best for all photovoltaic technologies at 1 Sun illumination [55]. However, the fabrication of such cells is complicated because only a small lattice mismatch between different materials can induce a high density of defects, detrimental for the cell. As a result, these type of solar cells are highly expensive, and therefore mainly used in specialized circumstances where a high power density is needed and cost is not critical, such as space applications [56].

At present, Si solar cells dominate the market because it is a mature technology. However, their efficiencies are still a bit from the Shockley-Quiesser limit and have not made significant progress for a long time [57]. Many new solar cell technologies have emerged the latest decades, with the ambition of outperforming the existing Si technology and make solar cells really competing with non-renewable sources. Two main strategies are used, either lower the cost so much that the PCE is not critical, or increase the PCE. In the next section, we shall see that nanowire solar cells have the potential of doing both.

## 3.4 Design and function of nanowire solar cells

The term nanowire solar cell refers to a photovoltaic device where arrays of semiconductor nanowires are the main and active component, responsible for the absorption of photons and the generation and separation of charge carriers. A typical design of such a device is shown in Figure 3.8 (a). Here arrays of vertically aligned nanowires are standing on a substrate. Each nanowire contains a charge separating p-n [58] or p-i-n junction [59], either in the axial [60] or radial direction [61], see Figure 3.8 (b). The back contact is typically established through a metal contact to the

substrate. The front contact usually consists of a layer of transparent conductive oxide (TCO) such as indium tin oxide or aluminum zinc oxide [62], deposited at the top surface of the nanowires. If any metal seed particle is still remaining at the top of the nanowires from the growth process, this is usually removed by wet etching before establishing contact, in order to avoid light reflection [63], [64]. For mechanical stability and electrical insulation, the nanowire arrays are usually embedded in a transparent polymer such as benzocyclobuten [65], [66], only exposing the tip to the TCO.

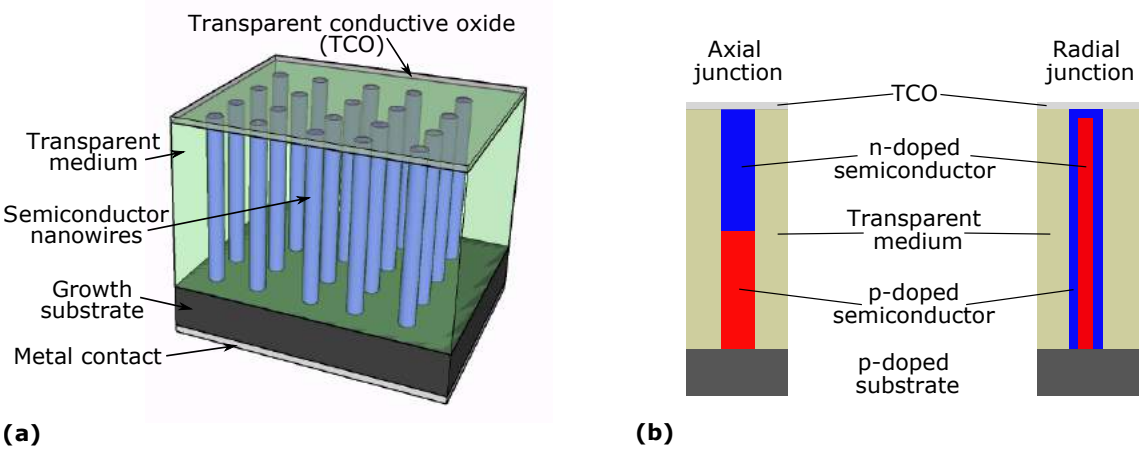


**Figure 3.8:** **(a)** Schematic structure of a nanowire solar cell. **(b)** Schematic illustraion of the difference between the axial junction geometry and the radial junction geometry

In conventional solar cells, the absorbtion of sunlight scales linearly with the projected area of the cell. This is intuitive and one can describe the situation with ray optics. The rays from the sun that do not hit the surface have no chance of becoming absorbed in the material. The situation becomes quite different for subwavelength structures. In this case, the wave nature of the light can give rise to resonance effects, dependent on the size, shape and chemical composition of the structures. Such resonance effects may confine the light within the structure and enhance the absorption. It has been shown that semiconductor nanowires with diameters of a few hundred nm exhibit this sort of resonance effects. In fact, it has been experimentally shown that a single, vertical GaAs nanowire can absorb sunlight corresponding to an area approximately 8 times larger than its physical cross sectional area [67]. This decoupling of the absorption and physical cross section means that a single nanowire solar cell can have a theoretical apparent efficiency >100% [68]. Of course, such efficiencies are not possible in large-area solar cells composed of nanowire arrays, because in that case also the area between the nanowires are included in the efficiency-calculation. Nevertheless, the waveguiding resonance effect enables a nanowire array (NWA) to be quite sparse and still absorb most of the incoming sunlight, see Figure 3.9. In fact, theoretical studies using finite-difference time-domain (FDTD) simulations have shown that a GaAs nanowire array with optimized diameter and pitch (distance between nanowires) can absorb more than 90% of the above-band gap incoming sunlight, which is significantly more than a

GaAs film of the same thickness (2 $\mu$m), even though the volume filling ratio of the NWA is only 0.196 [69]. This means that the material consumption could be reduced drastically in nanowire solar cells compared to thin films.

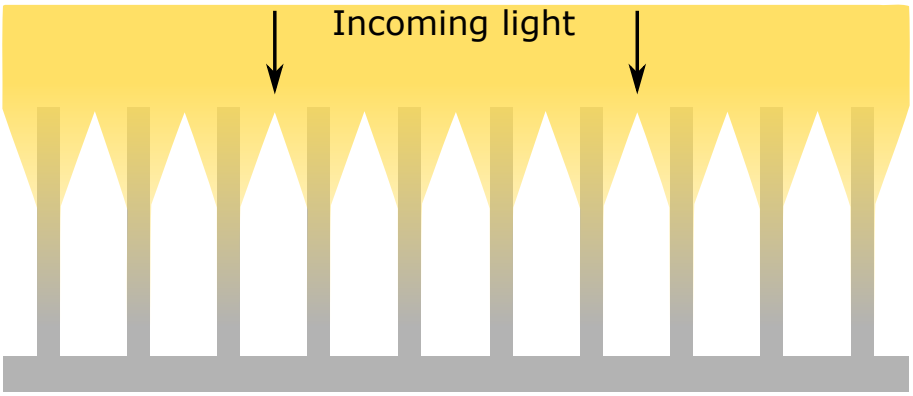


**Figure 3.9:** Enhanced absorption in nanowire array. Due to the wave nature of light and the sub-wavelength nanowire diameter, the nanowires act as waveguides for the incoming light and concentrates the light. This enables the nanowire array to absorb the incoming light without filling up the whole solar cell volume.

Another advantage with the nanowire design is that a NWA can have much lower reflectance than a thin film. This is because the effective refractive index of a NWA is lower than for a bulk sample of the same material [70]. The more sparse the NWA is, the closer the effective refractive index will be to 1 as that of the surrounding air. It is also possible to make conical nanowires to make a graded-index anti-reflective coating [71]. Dual-diameter [72] or base-tapered [73] nanowires can be used to optimize the absorption and material usage.

The radial junction geometry offers a potential advantage over planar junctions, since it decouples the optical and electrical thickness of the solar cells. This means that the nanowires can be made long, ensuring full absorption of the incoming light, without increasing the diffusion path lengths for the generated charge carriers. However, the radial junction geometry also implies a large junction area, which increases the $I_S$ of the cell [74].

Furthermore, in a conventional solar cell with a non-active absorbing substrate, a large portion of the photons generated by radiative recombination will be emitted into the substrate and not contribute to the output power [49]. In a nanowire solar cell though, fewer photons will be emitted into the substrate due to the waveguiding effect. This leads to an increased open circuit voltage, and as a result, the Shockley-Queisser limit for a NWA can be higher than the equivalent thin film cell [75]. Tapered nanowires can even be used to guide the emitted photons back in the opposite direction of the incoming photons, reducing the entropy losses associated with randomly emitted photons, thus further improving the optimal efficiency of nanowire solar cells [76].

Another limitation with thin-film solar cells is that there has to be a high match between the lattice parameter of the growth substrate and the active layer to avoid high concentrations of detrimental dislocations [77]. As a consequence, high-efficient III-V thin films are usually grown on substrates made of expensive materials such

as Ge. The lattice-matching constraint also severely limits the choices of material combinations in multijunction solar cells, where layers of different band gap need to be stacked upon each other [78]. In nanowire solar cells though, highly lattice mismatched structures are possible because the high surface-to-volume ratio of the nanowires enables efficient strain relaxation without dislocations [79]. For example, highly crystalline nanowires composed of GaAs [80], InP [81] and GaAsP [82] can be grown on inexpensive Si substrates. This lowers the cost and opens up the possibility for tandem junction solar cells [83].

There are many advantages with the nanowire design but there are also some drawbacks. The large surface-to-volume makes the nanowire solar cell vulnerable to surface recombination. Surface cleaning and passivation have been successfully applied to mitigate this [84], [85], [86], however there is a need for further understanding and improvement of surface passivation [87]. Furthermore, the small volume of the nanowires puts high demands on the control of the doping distributions, especially in nanowires with radial junctions where the thin layers are at risk of getting fully depleted. Even if separate solutions have been found to many of the critical issues, a remaining challenge is to combine them in a single device. In order to utilize the full potential of nanowire solar cells, one needs to optimize both the photonic properties by controlling the geometrical parameters of the NWA, and the electronic properties by having a high degree of control over doping and contact formation, all while keeping the fabrication cost low [74]. One prerequisite for developing nanowire solar cells is establishing versatile and reliable techniques for characterization and assessment of individual nanowires, which the next section will address.

## 3.5 Characterization of nanowire solar cells

Assessment measurements under standardized conditions on full nanowire array cells are important to provide a fair comparison to other solar cell techniques [88], however, they give limited insight to what needs to be optimized in order to increase the efficiency further. There is a need to be able to investigate the properties of individual nanowires since they are the building blocks of the solar cells. Of course, the small size of nanowires makes it challenging to study them. One common approach is to transfer a single nanowire from the growth substrate and place it horizontally on an insulating substrate, see Figure 3.10 (a). Electrical contacts to both ends of the nanowire can then be established by electron beam lithography and metal evaporation. In the case of radial junction nanowires, an additional step is required where the core is revealed by an etching process at one end of the nanowire, in order to contact both sides of the junction [89]. This setup is well suited for characterization of electrical properties inherent to the nanowires, such as I-V characteristics [90], charge generation and collection [86] and minority carrier diffusion lengths [91]. However, regarding characterization of optical properties, results obtained from horizontal nanowires will not be directly comparable to vertical nanowires since the waveguiding resonance effects differ significantly between the two geometries [92], [93].

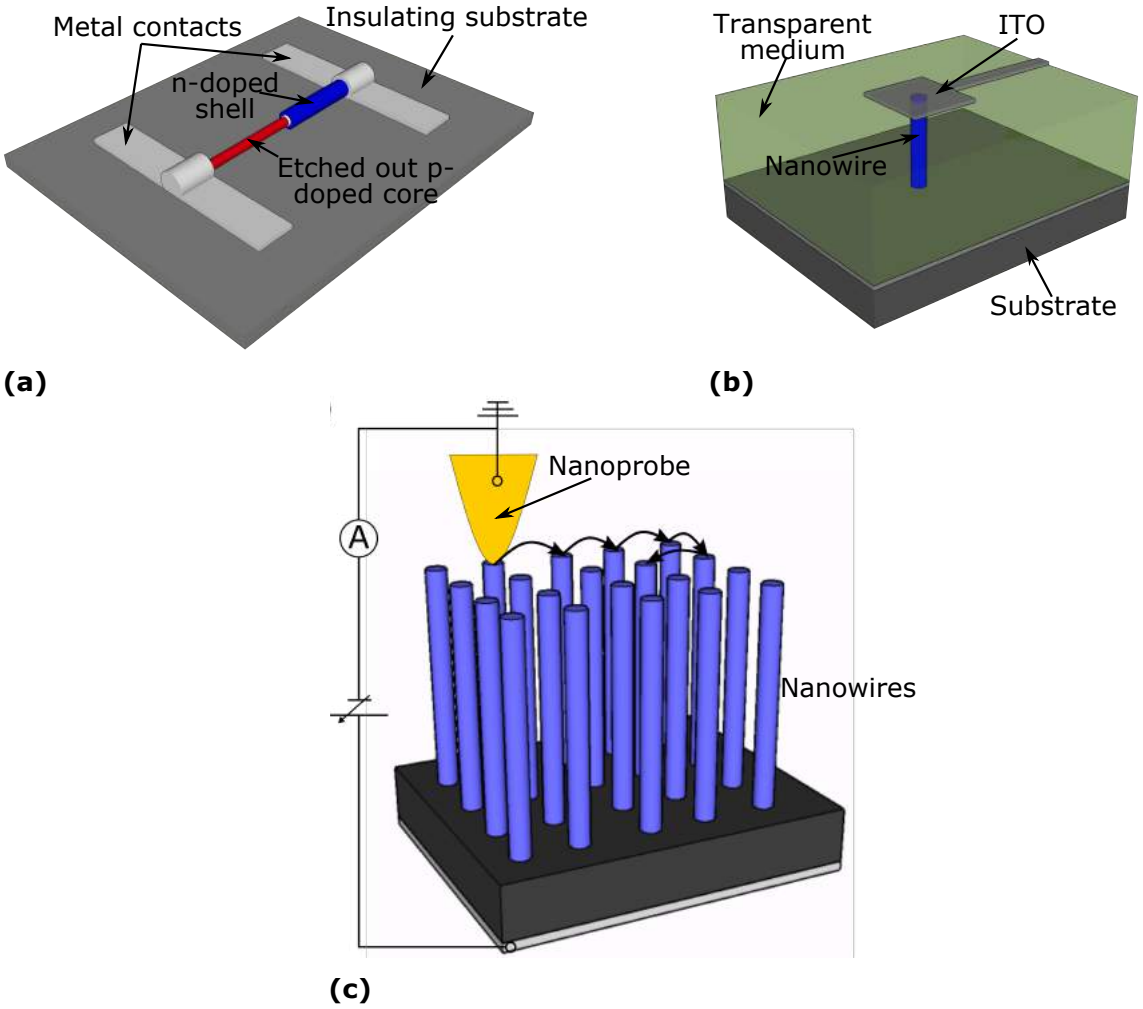


**Figure 3.10:** Three different techniques for characterizing single nanowire solar cells.

Another way to characterize individual nanowires is to fabricate a complete solar cell containing only one single nanowire, see Figure 3.10 (b). In this way, the optical properties in the vertical geometry may be studied in detail, and the strong light trapping effect may be observed [67], [94]. However, rigorous sample preparation is needed for each nanowire to be studied.

A third way to characterize individual nanowires, and the method used in this thesis, is to use an in situ nanoprobing instrument, see Figure 3.10 (c). In this way, individual nanowires in array samples can be selected and contacted with high precision. With this method, charge collection properties [95], [96] and I-V characteristics during both dark and illuminated conditions of single solar cell nanowires can be studied [97]. In Paper I, we describe this technique in detail and use it to study single GaAs nanowire solar cells. The advantage of this method is that the measurements can be carried out directly on nanowire array samples without the need of special sample preparation. Furthermore, the effect of mechanical strain on the properties of nanowire solar cells may be investigated by this technique. However, care must be taken to ensure a stable mechanical and electrical contact between the nanowire and the nanoprobe, in order for the results to be representative of

the nanowire properties. This can be especially challenging for self-catalyzed grown nanowires that lack a metal seed particle at the top.

## 3.6 Strain engineering of nanowire solar cells

As discussed in Section 2.3, extensive research has been carried out regarding the effect of strain on electrical and optical properties of semiconductor nanowires. Many of these effects could potentially be utilized in nanowire solar cells. For example, the ability to tune the band gap energy can be very advantageous since it dictates which photons that can get absorbed and how much of their energies that gets used. Despite this, reports of strain engineering applied to nanowire solar cells are scarce. Compressive strain has been shown to increase the photovoltaic efficiency of single $Cu_2S$/CdS nanowires by the piezo-phototronic effect [98]. Likewise, the same effect has been utilized in ZnO nanowire arrays to enhance the performance of Si-based solar cells [99]. Furthermore, a theoretical study has shown that compressive strain may increase the efficiency of GaAs nanowires containing both ZB and WZ segments [100]. In paper III, we study the effect of mechanical strain on the electrical and photovoltaic properties of GaAs nanowire solar cells.

# 4. Metal-semiconductor contact

High quality metal-semiconductor contacts are essential for semiconductor technology. All semiconductor devices generally need to be connected to a metal-based electrical circuit, either for power supply, signal processing or energy harvesting. This chapter describes the formation and electrical behaviour of Ohmic and Schottky contacts, and accounts for a theoretical model of current flow through a Schottky barrier. In the end, the detrimental effect of a Schottky barrier on p-n junction based photovoltaics is discussed.

## 4.1 Ohmic contact

Ohmic contacts are characterized by low resistances and linear I-V characteristics. For most applications, Ohmic contacts are desirable, since they do not affect the overall I-V characteristics of the device. However, at a metal-semiconductor interface an energy barrier, which obstructs the flow of charge carriers, is often formed due to the band gap of the semiconductor. The height of the barrier is usually dependent on the work function of the metal and the electron affinity of the semiconductor [45]. In some cases, an Ohmic contact may be achieved by choosing a metal with a work function lower than the electron affinity of the semiconductor. However, in many cases the Fermi level of the metal tend to align within the band gap of the semiconductor, forming a barrier regardless of the metal work function [101]. Instead, the most common way to achieve Ohmic metal-semiconductor contacts is to create a high doping concentration in the semiconductor locally at the contact. This is typically done by deposition of several layers of suitable metals (Pd/Ge/Au for n-doped GaAs), followed by an annealing process where the metal diffuses into the semiconductor [102]. In this way, the barrier becomes so narrow that electrons may easily tunnel through, and high currents may flow in both directions. While this approach usually results in high quality Ohmic contacts, it may be difficult to implement, especially in nanoscale applications.

## 4.2 Schottky contact

As opposed to an Ohmic contact, a Schottky contact is current rectifying and has non-linear I-V characteristics. A Schottky contact is usually formed if the semiconductor has low doping and the Fermi level of the metal is within the band gap of the semiconductor.

If an n-doped semiconductor with a high Fermi level and a metal with a lower Fermi level are brought into electrical contact, electrons will flow from the semiconductor to the metal until an equilibrium is reached and the Fermi levels of the two materials are aligned. This will leave immobile positive ions in the depleted region

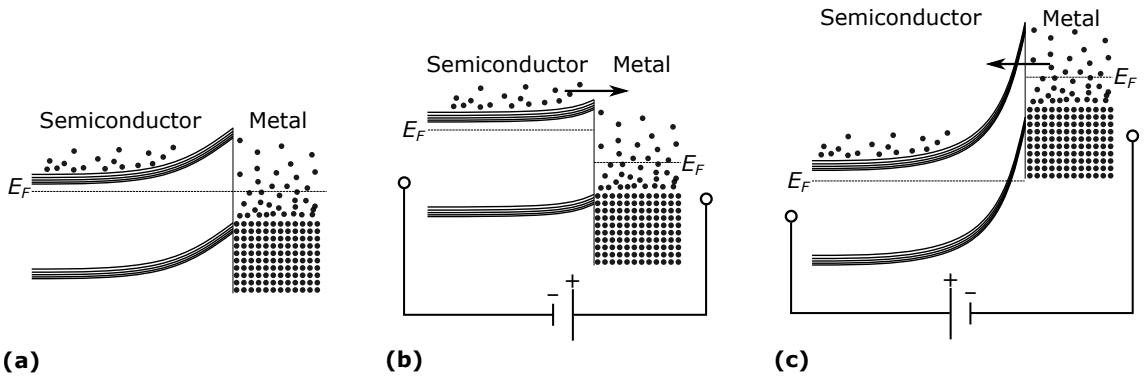


**Figure 4.1:** Metal-semiconductor Schottky contact in **(a)** equilibrium. The Fermi levels are aligned and the conduction and valence bands are bent close to the interface of the two materials, creating an energy barrier for the electrons. **(b)** Forward bias state. The energy barrier is lowered by the applied bias, and the electrons from the semiconductor can go over the barrier. This process is called thermionic emission. **(c)** Reversed bias state. The energy barrier is increased by the applied voltage and the electrons can no longer go over the barrier, but could tunnel through the barrier. This is the so called thermionic field emission process.

of the semiconductor, giving rise to a built-in field and a bending of the conduction and valence band energies [45], see Figure 4.1 (a). The slope in the band energies of the semiconductor forms a barrier for the electrons. Under forward bias conditions, i.e when an external bias is applied with the positive pole connected to the metal, the barrier is lowered and thermally excited electrons in the semiconductor can go over the barrier into the metal, as in Figure 4.1 (b). This is called thermionic emission (TE) [103] and is described by

$$I = SA^*T^2\exp\Big(-\frac{\phi_b}{k_BT}\Big)\exp\Big(\frac{qV}{nk_BT}\Big) \times \Big\{1 - \exp\Big(-\frac{qV}{k_BT}\Big)\Big\}, \tag{4.1}$$

where $I$ is the current, $S$ the area of the contact, $A^*$ is Richardson's constant, $T$ the temperature, $\phi_b$ is the barrier height, $k_B$ is Boltzmann's constant, $q$ is the elementary charge, $n$ the ideality factor and $V$ is the applied bias. Under reverse bias conditions, however, the barrier height will increase and the electrons cannot go over the barrier. This results in a current rectifying behaviour of the contact if only thermionic emission is considered. However, in many cases there is a significant current flowing even in the reverse bias state, especially in nanoscale applications [104]. The reason for this is that there is a possibility for the electrons to tunnel through the barrier, see Figure 4.1 (c). This phenomena is described by thermionic field emission (TFE) theory [105], which states that the current through a Schottky barrier is given by

$$I = I_{sb}(V, \phi_b) \times \exp\Big\{V\Big(\frac{q}{k_BT} - \frac{1}{E_0}\Big)\Big\} \tag{4.2}$$

where the saturation current $I_{sb}$ can be expressed as

$$I_{sb} = \frac{SA^*T(\pi qE_{00})^{1/2}}{k_B}\exp\left(-\frac{\phi_b}{qE_0}\right) \times \left\{q(V-\xi) + \frac{\phi_B}{\cosh^2(qE_{00}/k_BT)}\right\}^{1/2}. \quad (4.3)$$

Here $\xi$ is difference in energy between the Fermi level and the bottom of the conduction band. $E_0$ can be expressed as

$$E_0 = E_{00}\coth\left(\frac{qE_{00}}{k_BT}\right) \quad (4.4)$$

and

$$E_{00} = \frac{\hbar}{2}\left(\frac{N_d}{m_n^*\epsilon}\right)^{1/2} \quad (4.5)$$

whith $N_d$ being the doping concentration, $m_n^*$ the effective electron mass and $\epsilon$ is the permittivity. In Figure 4.2 it is evident that the TFE model gives a significantly larger current during reverse bias than the TE model.

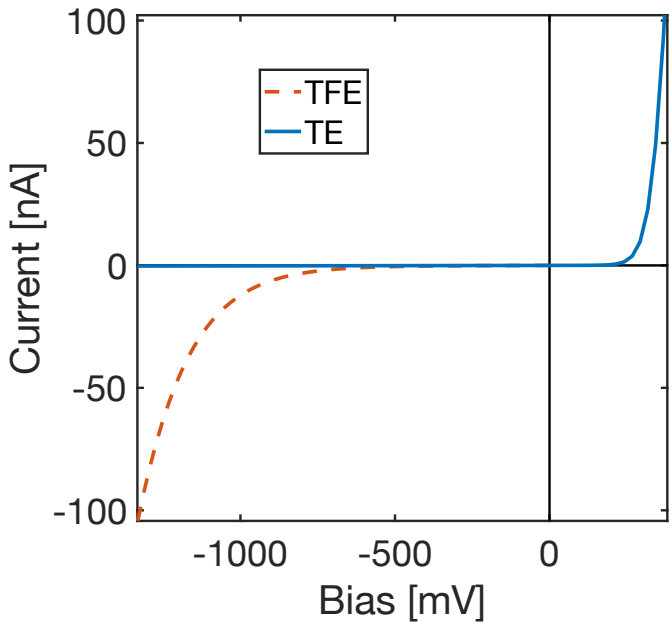


**Figure 4.2:** Modeled I-V characteristics of a Schottky diode using TE and TFE, respectively.

### 4.2.1 Surface defects and insulating layer

In practice, a thin insulating layer is often present between the metal and the semiconductor. For example, if III-V nanowires are exposed to air, they usually get covered with a thin native oxide layer. If this oxide layer is not removed before contacting the nanowire, it increases the distance between the semiconductor and the metal, which reduces the probability of tunneling, see Figure 4.3 (a). The effect

of an insulating layer with a thickness $\delta$ and a mean barrier height $\chi$ may be taken into account in the model by incorporation of an effective Richardson's constant $A^{**}$defined as [104],

$$A^{**} = A^{*}\exp(-\chi^{1/2})\delta. \tag{4.6}$$

In Figure 4.3 (b) it can be seen that the thickness of the insulating layer affects the current significantly.

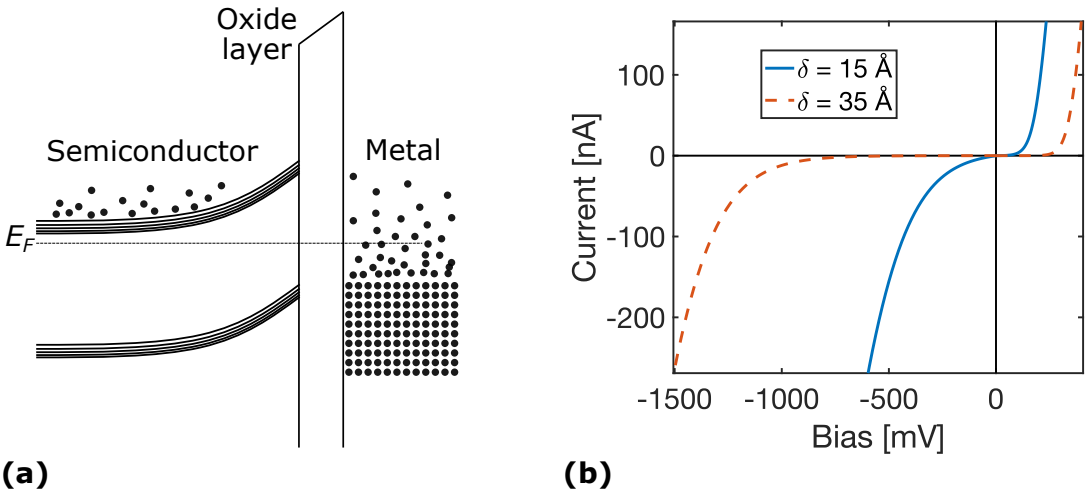


**Figure 4.3:** **(a)** Band diagram of a Schottky contact with a thin insulating layer present between the semiconductor and the metal. **(b)** I-V characteristics of a Schottky contact with with a thin insulating layer of thickness 15 Å and 35 Å, respectively.

There may also be localized electronic states at the interface between the semiconductor and the metal, that introduce an alternative current path, which can be considered as a shunt resistance in parallel with the Schottky barrier. This will lead to linear I-V characteristics at very small biases [106].

### 4.2.2 Combination of a p-n junction and Schottky barrier

High quality contacts are crucial for the performance of solar cells. However, it is common that an unwanted Shottky barrier is formed at the contact, especially for in situ measurement of single nanowires where optimal contact formation may be obstructed by the complexity of the experimental setup. Figure 4.4 shows an example of modeled dark and illuminated I-V characteristics of a p-n junction with Ohmic contact and a p-n junction with a Schottky contact.

The dark current is significantly reduced by the Schottky barrier. The illuminated I-V curve is affected even more. Instead of being a superposition of the dark I-V curve, it has an S-shape around zero bias. This rather peculiar feature is qualitatively explained by the band diagrams shown in Figure 4.5. If the p-n junction is combined with a Schottky contact with an insulating oxide layer on the n-side, there will be two slopes in the bands with opposite direction. When the p-n junction is reversely

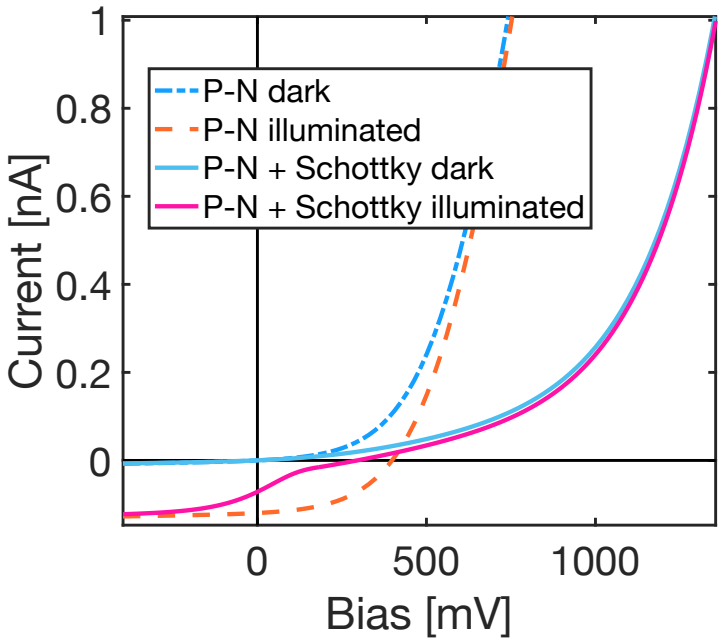


**Figure 4.4:** Modeled I-V characteristics of a P-N junction with Ohmic contact and a Schottky contact, in dark and illuminated condition, respectively. The rectifying behavior of the Schottky barrier reduces the forward current and introduces a kink in the illuminated I-V curve.

biased [Figure 4.5 (a)], the Schottky barrier is forwardly biased and the barrier height at the contact is lowered, letting through the photogenerated charge carriers. However, when the p-n junction is forwardly biased [Figure 4.5 (b)], the height of the Schottky barrier increases as it is reversely biased. The photogenerated charge carriers are blocked by the barrier and the oxide layer, and the photocurrent is significantly reduced.

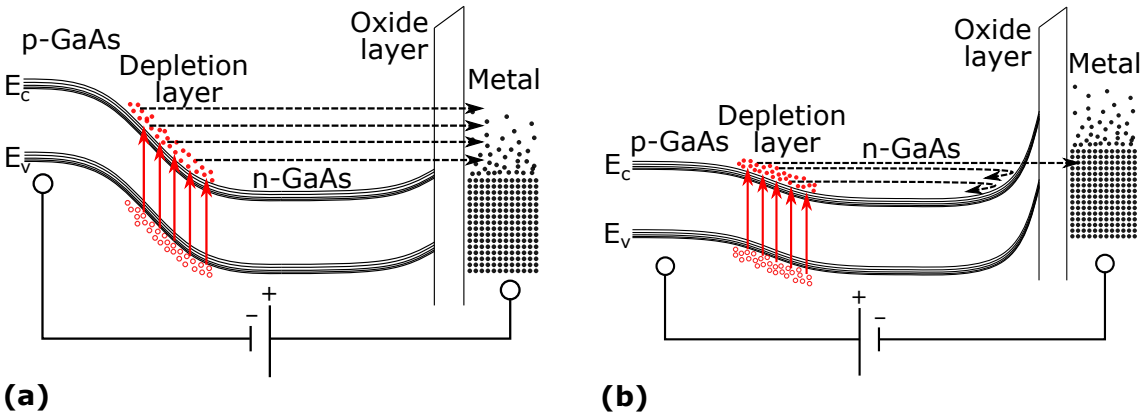


**Figure 4.5:** **(a)** Band diagram of a reversely biased, illuminated p-n junction in series with a Schottky barrier with an insulating oxide layer. The Schottky barrier height is reduced by the applied bias and the photogenerated charge carriers can tunnel through the oxide layer. **(b)** Forwardly biased, illuminated p-n junction in series with a Schottky barrier with an insulating oxide layer. The Schottky barrier height is increased by the applied bias and the photogenerated charge carriers cannot tunnel through both the oxide layer and the Schottky barrier.

# 5. Experimental techniques, methods and materials

## 5.1 Scanning electron microscopy

The general construction of a scanning electron microscope (SEM) is shown schematically in Figure 5.1. An electron gun is located at the top of the instrument where electrons are emitted and accelerated downwards by an electric potential in the order of 1-30 keV. An electrostatic gun lens gathers the electrons into a crossover-point, and this crossover is subsequently de-magnified by a set of electromagnetic lenses located further down a cylindrical space commonly known as the "column" of the microscope. Unlike glass lenses, the focal length of an electromagnetic lens can easily be altered by changing the current running through its coil. In this way, the de-magnification of the crossover and the lateral point where the beam is in focus can be changed simply by turning a knob changing the coil current. As the electrons travel down the column they also pass through a number of apertures with variable sizes that control the current and the convergence angle of the beam. The column also contains a pair of so called scanning coils. Their task is to deflect the beam so that it is scanned over a certain area of the specimen. The objective lens, located at the bottom of the column, is used to focus the beam on the surface of the specimen, which generally is located around 2-50 mm below the polepiece of the objective lens. Once the electron beam hits the sample, various signals are generated due to interactions between the beam electrons and the sample. These signals carry different information and can be used to form an image of the specimen, but also for spectroscopy determining elemental composition, diffraction for crystallographic characterization etc. [107].

### 5.1.1 Imaging

In the image formation process, the beam is scanned over an area of the specimen in an x-y pattern. The beam stops for a certain amount of time, typically in the µs range, at a discrete set of points on the specimen. Simultaneously, an image is built up on a computer display where the pixels have a one-to-one correspondence to the beam locations on the specimen. The brightness of each pixel is determined by the strength of the signal that is chosen to be collected. Most SEM images generated in this way tend to be surprisingly intuitive to interpret. However, a basic knowledge of the signal generation and detection, image formation and contrast mechanisms helps to correctly interpret the fine details.

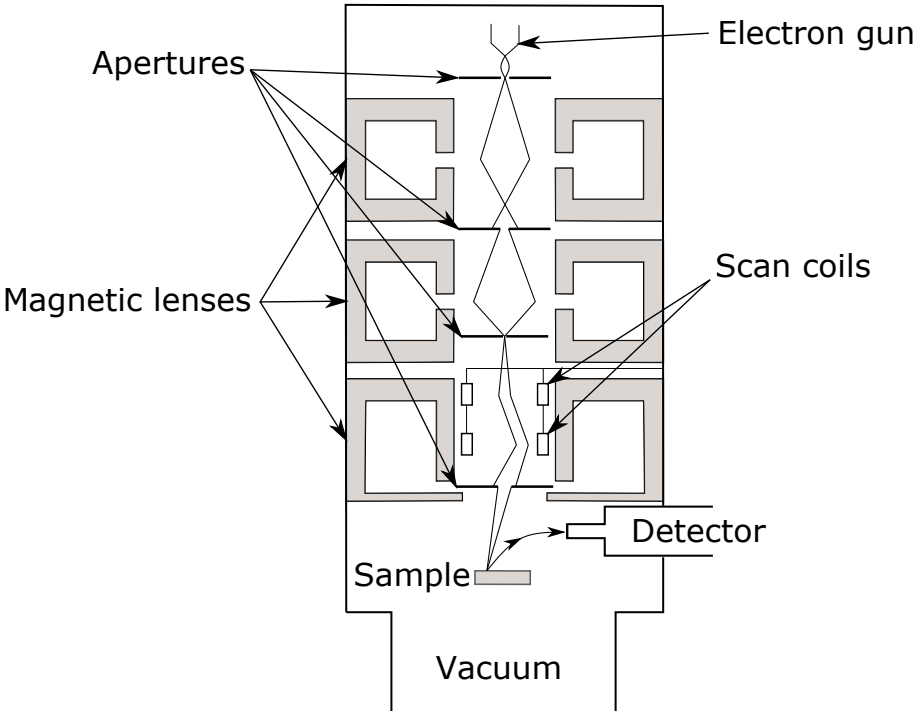


**Figure 5.1:** Schematic structure of an SEM. An electron gun produces an electron beam that is accelerated down through the column by an electric field. An electrostatic gun lens forms the first cross-over. A set of apertures and electromagnetic lenses are used to further de-magnify the beam diameter, and a set of scan coils are used to scan the beam across the sample. Various signals are generated from the beam-sample interaction and detected to form an image or provide other information of the sample.

The two main signals used for image formation are so-called backscattered electrons (BSEs) and secondary electrons (SEs). BSEs are primary electrons (electrons from the beam) that due to both elastic and inelastic collisions with the atomic nuclei in the sample changes their traveling direction and eventually escape the sample more or less in the opposite direction of the beam. When these BSEs leave the sample their kinetic energies range from almost zero up to the energy of the incoming electrons (1-30 keV). A consequence of the collisions is that the beam broadens on its way through the specimen. The corresponding volume is called the beam interaction volume, see Figure 5.2 (a). The broadening lowers the imaging resolution for the BSE signal. The probability for the primary electrons to collide depends on the atomic number, Z, of the elements in the sample. Heavy elements generate a stronger BSE signal than lighter elements, and this phenomenon is the basis for a contrast mechanism called elemental contrast or Z-contrast. Furthermore, the BSE signal has a significant directionality, and tends to be strong along the direction of the specimen normal. This may give rise to a topographic contrast [108].

SEs are electrons that are knocked out from the sample atoms due to inelastic collisions of the primary electrons. The SEs are generated throughout the whole interaction volume. However, SEs have small kinetic energies, $E_k < 50$ eV, and therefore short mean free paths in the sample. Thus it is only those that are gen-

erated close to the surface that can escape the sample and give rise to a detectable signal [107]. The imaging resolution of the SE signal can therefore be close to the beam diameter, and for high quality SEMs a resolution of less than 1 nm can be reached [109]. As the tilt angle of the surface of the sample increases, the effective volume that lies within the escape range for the SE increases. Thus, highly tilted surfaces give rise to a strong SE signal. Edges, corners and small structures such as nanoparticles or nanowires also have a large effective volume within the escape range. A strong SE signal can therefore be expected at such positions, see Figure 5.2 (b). On the other hand, flat surfaces and valleys have small effective volumes within the escape range, resulting in a weak SE signal. This phenomenon gives rise to a topographic contrast, and the SE signal is therefore well suited to reveal the topography of the sample, with high spatial resolution.

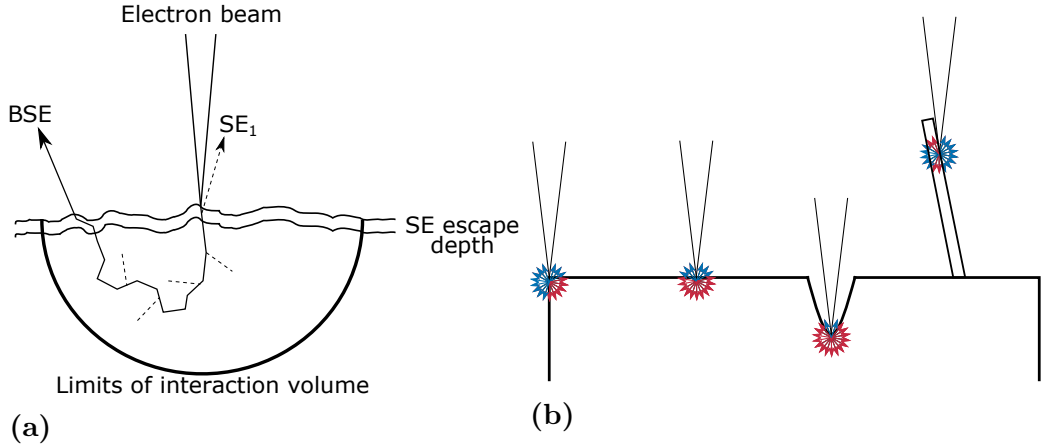


**Figure 5.2:** **(a)**: Qualitative illustration of the beam interaction volume in an SEM. Once the beam hits the sample it is broadened due to the interaction between the electrons and the atoms in the sample. This reduces the resolution of the BSE signal. SEs are also generated in the whole interaction volume, however, since it is only those SEs that are generated close to the surface that escape and get detected, the SE signal can have almost the same resolution as the beam diameter. **(b)**: Topographic contrast mechanism for SE. The blue arrows represent SE that can escape from the sample, and red arrows represent SE that stays in the sample. As can be seen, highly tilted surfaces, edges and corners result in high SE signal while flat surfaces and valleys result in low SE signal.

Once the SEs and BSEs have escaped the sample, they need to be detected in order to make use of the signals. The most common detector is the so-called Everhart-Thornley (ET) detector. It is usually placed above the sample, see Figure 5.3 (a). Both BSEs and SEs can be detected by the ET detector. If a negative bias >50 V is applied to the detector, all the SEs will be deflected and only the highly energetic BSEs with trajectories pointing towards the detector will contribute to the measured signal. The resulting image will therefore have Z-contrast (heavy elements will appear brighter than light elements), but also some topographic contrast were the surfaces tilted towards the detector will appear brighter than surfaces tilted away from the detector. For normal imaging though, the ET detector is usually positively

biased, with a potential of around 250 V. As a result, the low energy SEs are drawn into the detector, regardless of the direction of their original trajectories, see Figure 5.3 (a). The BSEs will still be detected, and the measured signal will be a mixture of both BSEs and SEs. Because of this additional SE signal, the image will gain extra topographic contrast. Any tilted surface, edge, corner, peak or nanoparticle will appear bright, whether its facing the detector or not. In order to understand or imagine how the final image will look like, there is an analogy that can be made between the situation in the microscope and an everyday life situation, see Figure 5.3 (b). The image will appear as though the the viewer were looking down on the sample along the direction of the beam, and the sample was both illuminated by diffuse light and a highly directional light source located at the detector. The directional light source represents the BSE signal and the diffuse lighting represents the SE signal. This is what we are used to since the sun is a directional light source and the scattered light from clouds and objects provides diffuse illumination of our environment, which is why SEM images generated in this way are so easy to interpret [107]. However, there are other ways of forming images, using other types of detectors and signals, which may be more difficult to interpret. In this thesis though, all the SEM images were generated in the way described above, with a mixture of SE and BSE signals.

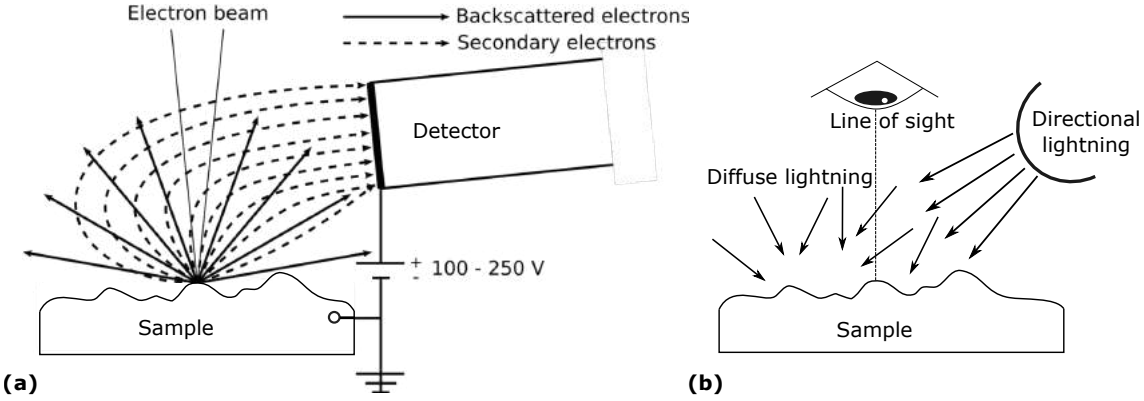


**Figure 5.3:** **(a)** Detection of BSE and SE with an ET detector. By applying a positive bias to the detector, the low-energetic SE will be drawn into the detector while the high-energetic BSE will be unaffected. **(b)** Real-life analogy of SEM images generated with a positively biased ET-detector. The images will appear as if the viewer is located at the beam source and the sample is illuminated with a directional light source (BSE signal) located at the position of the detector, and an additional diffuse lighting source (SE signal).

### 5.1.2 Electron beam induced current mapping

Electron beam induced current (EBIC) mapping is a technique that is used to map the electronic activity of a sample. When the electron beam is scanned across a semiconductor sample, electron - hole pairs will be created, just as when the sample is illuminated by photons. The difference is that the electron beam is localized to a spot size of a few nanometers. If, for example, a p-n junction is present, the electron-hole pairs will be separated and generate a current. Since the beam-electrons in an

SEM generally have energies in the range $0.1 - 30$ keV, and typical semiconductor band gap energies are $\sim 1$ eV, each beam-electron can potentially generate thousands of electron-hole pairs. The measured current will therefore depend on the beam-current, but with a large amplification. By plotting the measured current over the analyzed area pixel by pixel, an EBIC map will be created. If the amount of generated electron-hole pairs is the same in each pixel, the EBIC signal will represent the fraction that are separated and contribute to the current before recombining. Parameters that may influence this are the quality of the p-n junction, the electron and hole diffusion length and distance to reach the junction, and the crystalline quality of the sample (defects act as recombination centers).

The amount of generated electron-hole pairs is largely dependent on the interaction volume of the beam electrons, and the topography of the sample. If the beam is placed close to the edge of the sample, so that part of the interaction volume is outside the sample, it means that some of the beam-electrons will escape before transferring all their energy to the sample. Fewer electron-hole pairs will therefore be created. Figure 5.4 shows Monte Carlo simulations of the interaction volume in a GaAs nanowire at a few different beam acceleration voltages. It is important to keep this in mind for correct interpretation of EBIC maps.

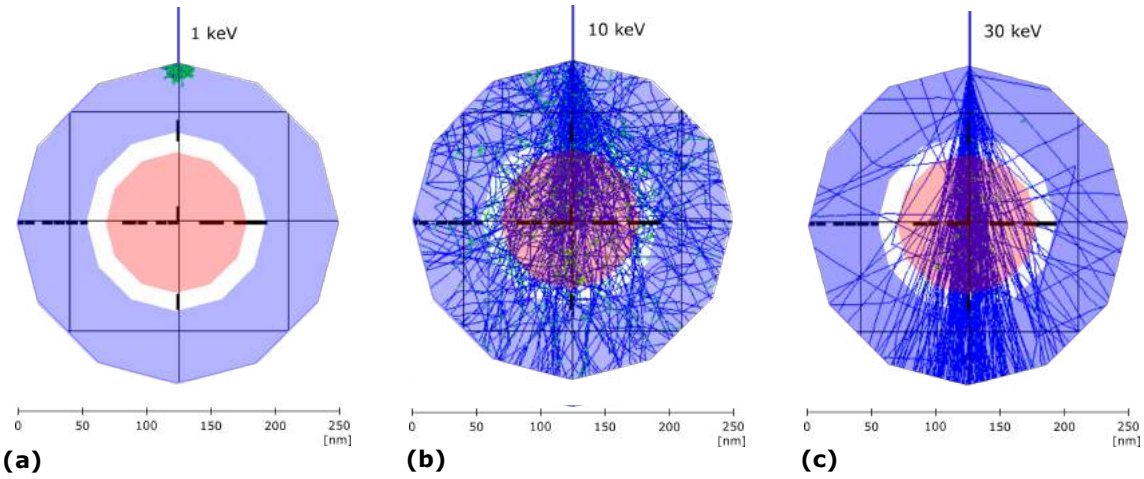


**Figure 5.4:** Beam interaction volume simulated using Monte Carlo model at beam acceleration voltage **(a)** 1 keV **(b)** 10 keV and **(c)** 30 keV

## 5.2 Transmission electron microscopy

In a transmission electron microscope (TEM), an electron beam is transmitted through, and detected below, the specimen. The sample needs to be thin, usually around 100 nm, in order for the electrons to be transmitted without too much interaction with the specimen. The resolution of a TEM is 1-10 Å, which means that the atomic structure of the sample can be investigated. The basic principle of a TEM is depicted in Figure 5.5 (a). An electron gun generates a current of electrons that are accelerated by an electric field of 50-300 keV. The electron beam then passes through the illumination system, which consists of an electrostatic gun lens and a number of condenser lenses and apertures. As in an SEM, the electromagnetic

lenses create a strong, adjustable magnetic field that affects the trajectories of the electrons. The apertures are discs with holes where the central part of the beam can pass through but the rest of the beam is blocked. The condenser lenses form either a parallel or convergent beam that illuminates the sample. For traditional TEM imaging and diffraction, a parallel beam is used. After the beam has passed through the specimen it enters the imaging system, also consisting of lenses and apertures. Their role is to magnify and project either an image or a diffraction pattern of the specimen onto a florescent screen or a charge-coupled device (CCD) camera [110]. Please note that Figure 5.5 (a) is a simplified version of an actual TEM, which generally has more lenses, apertures and components.

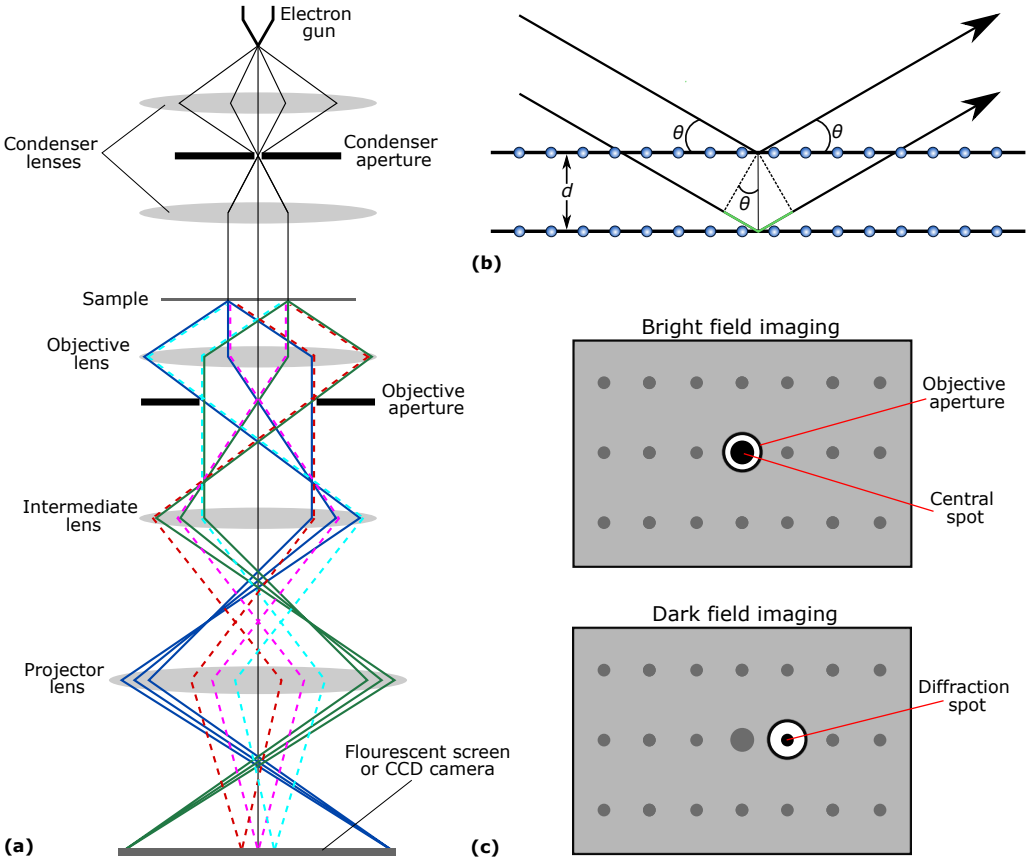


**Figure 5.5:** **(a)** Simplified schematic of a TEM. An electron gun emits electrons that are accelerated by an electric field. Condenser lenses and apertures are used to form a parallel beam that illuminates the sample. The electrons are scattered into different angles by the interaction with the sample. In imaging mode, electrons that emerge from one point on the sample (solid lines of same color) are gathered into one point on the screen or CCD camera by a set of lenses. In diffraction mode, it is instead electrons that are diffracted into the same angle (dashed lines of same color) that are gathered into one point. To toggle between the two modes, it is sufficient to change the strength of the intermediate lens. **(b)** Graphical description of Bragg's law. The incoming electron rays are reflected at the atomic planes. If $\theta$ is such that the extra distance the lower ray need to travel (green segment) equals an integer number of wavelengths, constructive interference occur and diffraction is obtained at that angle. **(c)** Principal behind BF and DF imaging. For BF the objective aperture is placed so that the central spot can pass through, while for DF one or more diffracted spots are chosen to pass through.

### 5.2.1 Diffraction

When the electrons are transmitted through a sample, they are scattered because of interaction with the atoms in the specimen. If the sample is crystalline, the atoms are ordered in a lattice with a certain periodicity. This results in certain preferred scattering angles of the electrons, a phenomenon called diffraction. The simplest way to describe diffraction is through Bragg's law. In this picture, the atomic planes are

regarded as mirror planes where the incoming electrons get reflected, see Figure 5.5 (b). In order for constructive interference to occur, the difference in traveled distance for electrons reflected at different atomic planes has to be an integer multiple, $n$, of the wavelength of the electrons. The angles $\theta$ that fulfill this requirement can be found using the Bragg equation:

$$2d \sin \theta_B = n\lambda. \tag{5.1}$$

Here $\theta_B$ is the Bragg angle, $d$ is the distance between two adjacent atomic planes and $\lambda$ is the wavelength of the incoming electrons. In a TEM, the kinetic energy of the electrons is known and controlled by the acceleration voltage, thus $\lambda$ can be calculated, and $\theta$ can be measured. Diffraction can therefore be used to investigate the spacing between atomic planes of crystalline samples. In fact, it is possible to find the complete crystal structure of the specimen by analysing so called diffraction patterns. The dashed lines in Figure 5.5 (a) shows how such a diffraction pattern is collected in a TEM. Basically, all the electrons that are diffracted along a certain angle are focused into a spot in the back focal plane of the objective lens. This plane is then chosen as the object plane of the projection lens, by adjusting the strength of the intermediate lens, and projected onto the viewing screen or the CCD camera. Each spot corresponds to one set of parallel atomic planes in the sample, except for the central spot which corresponds to electrons that have been transmitted through the sample without being scattered. The distance between a diffraction spot and the central spot is reversely proportional to the distance between the atomic planes corresponding to that diffraction spot. The symmetry of the diffraction pattern is related to the symmetry of the crystal structure of the specimen [110].

### 5.2.2 Imaging

In a TEM, an image is produced by focusing all the electrons scattered from one point in the sample to one point at the viewing screen or CCD camera. This is done by adjusting the strength of the intermediate lens so that the image plane of the objective lens becomes the object of the projector lens, see the solid lines in Figure 5.5 (a). There are two different modes of imaging typically used in a TEM, bright field (BF) and dark field (DF). It is the position of the objective aperture relative to the diffraction pattern that determines whether the resulting image is a BF or DF image, see Figure 5.5 (c). The objective aperture is located at the back focal plane of the objective lens, which is a conjugate plane of the diffraction pattern. This means that by varying the size and position of the objective aperture, one can choose which diffraction spots will be blocked and which ones that will pass through the aperture and contribute to the final image. If the central spot, corresponding to unscattered electrons, is chosen to pass through the aperture, the resulting image will be BF. Thin, low-mass areas of the specimen that do not scatter the electrons so much will appear bright, while thicker, high-mass areas will appear dark in a BF image. If instead the central spot is blocked and only one or more of the diffracted beams are chosen to pass through the aperture, a DF image will be produced. Then areas that diffract electrons into the chosen spots will appear bright while other areas will appear dark. This is especially useful when the specimen contains regions

with different crystal structure or orientation, such as polycrystalline or polytypic samples.

## 5.3 Focused ion beam - scanning electron microscope

A focused ion beam (FIB)-SEM is a dual beam instrument with both an electron beam column and an ion beam column. The two columns are tilted with regards to each other, normally at an angle of $\sim 50°$, see Figure 5.6. The advantage of such an instrument is that the high-resolution imaging capability of the SEM is combined with the sputtering capability of the FIB. When the ions hit the sample, atoms located close to the sample surface will be sputtered away. In this way, the FIB can be used to remove unwanted material and mill structures in the sample with high precision, while the process is being monitored using the SEM image. TEM-lamellae with thicknesses $< 100$ nm can be routinely prepared using FIBSEM. An issue with this technique is that ions from the beam can get implanted in the sample and crystalline samples may undergo a transition to an amorphous phase close to the milled surface. These unwanted features can, to a certain degree, be limited by adjusting the acceleration voltage and current of the ion beam.

Most FIBSEM:s also contain a gas injection system (GIS). A precursor gas is injected close to the sample surface, where the gas molecules are adsorbed. However, the molecules only decomposes where the electron or ion beam hits the sample. This enables local material deposition, spatially controlled by either the electron or the ion beam. Both conductive and insulating materials can be deposited this way [111].

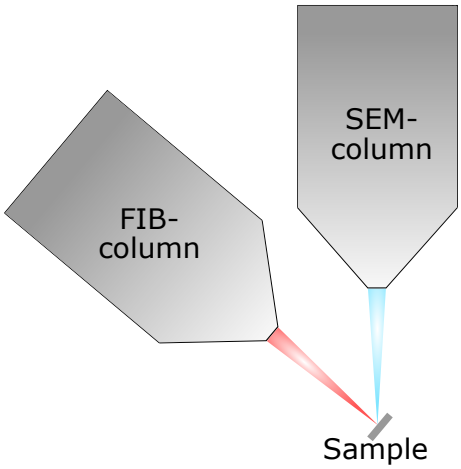


**Figure 5.6:** Schematic illustration of a FIBSEM. The instrument contains both an SEM-column and a FIB-coulmn, tilted approximately 50° with respect to each other. The ion beam may be used to sputter material from the sample while the electron beam is used for imaging.

## 5.4 In situ STM–SEM setup for SEM and FIB-SEM

In a scanning tunneling microscope (STM), a sharp, conducting nanoprobe is scanned closely above the surface of a sample while the measured tunneling current is used to produce an image of the surface. For in situ STM-SEM however, the imaging is provided by the SEM, while the STM is used for electrical measurements of nanoscale objects. For the in situ measurements of this work, an STM merged together with a SEM sample holder was used, see Figure 5.7. The SEM-holder makes it possible to place the STM and the sample inside the vacuum chamber of an SEM or a FIBSEM. A light emitting diode (LED) is mounted on the holder to provide light illumination of the sample.

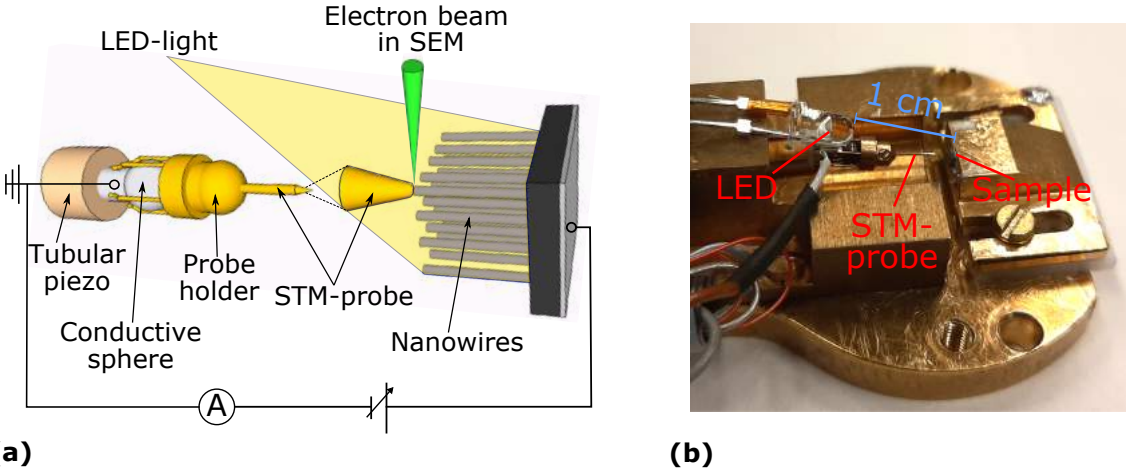


**Figure 5.7:** **(a)** Schematic illustration of the STM-SEM holder. Reprinted with permission from Nano Energy, 53, 2018, 175-181 (Paper I). Copyright Elsevier 2018. **(b)** Photograph of the STM-SEM sample holder used for the experimental work. The LED is mounted above and behind the STM-probe, approximately 1 cm away from the sample.

The STM is composed of a tubular piezo that controls the 3-dimensional movement of a conductive sphere. A six-legged metal probe-holder is clamped to this metal sphere. The probe is attached to the probe-holder, and the sample is placed within reach of the tip of the probe. The sample and the probe are connected to an external electrical circuit containing a picoammeter and a power supply. By moving the probe into contact with a specific part of the sample, for example a nanowire, the electrical circuit can be closed and measurements may be performed.

The movement of the STM probe has two different modes, coarse movement and fine movement. In the fine movement mode, the spatial resolution is $\sim$ 1 nm, but the range is limited to around 1 µm for backward/forward movement and around 10 µm for upward/downward and side movement. The coarse movement mode provides a range of several millimeters in all directions, but with a lower spatial resolution.

The sharp tip of the STM-probe can be produced by cutting a 0.25 mm gold wire with a clean pair of scissors, simultaneously as the gold wire and scissors are being

pulled apart. This produces an uneven cut area which usually contains features sharp enough for contacting a single nanowire.

A schematic illustration of the in situ experimental setup for nanowires is shown in Figure 5.8 (a). After the STM-probe has been moved into contact with the tip of a single nanowire, Pt-deposition enabled by the GIS of the FIBSEM is used to weld the STM-probe to the nanowire. This stabilizes the contact and enable strain to be applied to the nanowire by moving the STM-probe. The external circuit enables current-voltage (I-V) measurements. As the LED is switched on, photons will be emitted and absorbed in the nanowire and create electron-hole pairs, which are separated by the p-i-n junction within the nanowires. In order to analyze the single nanowire I-V characteristics quantitatively, the electrical circuit shown in 5.8 (b) is used to model the system. The nanowire is represented by a p-n diode ($D_1$), a current generator ($I_{ph}$) , a shunt resistance $R_{sh}$ and a series resistance $R_{NW}$, just as in the single diode model for solar cells, and therefore equation 3.3 governs the current through the nanowire. The contact between the STM-probe/Pt-deposition and the nanowire is represented by a Schottky diode ($D_2$), since it is a metal-semiconductor contact, and a shunt resistance, $R_C$. The current through $D_2$ is governed by equation 4.2. Applying Kirchoff's voltage law to the circuit in 5.8 (b), we get

$$V = V_{contact} + V_{nanowire}. \tag{5.2}$$

By solving the system of equations 3.3, 4.2 and 5.2 numerically, we may find the total current through the circuit as a function of applied bias.

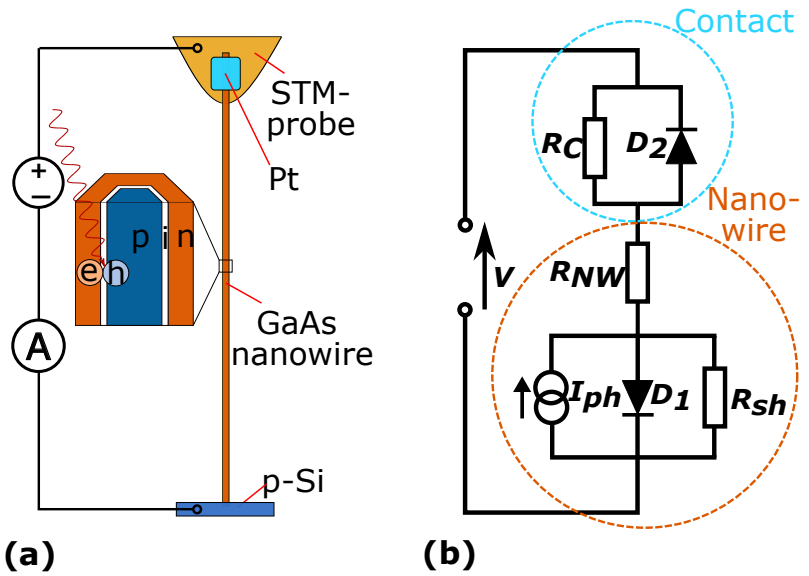


**Figure 5.8:** **(a)** Schematics of the experimental system. The STM-probe and the nanowire are attached through Pt-deposition. The external circuit contains a pi-coammeter and a power supply, enabling I-V measurements. Electron-hole pairs that are generated by absorption of photons from the LED gets separated by the built-in field of the radial p-i-n junction within the nanowire. **(b)** Equivalent electrical circuit of the experimental system. The contact is represented by a Schottky diode and a resistance in paralell. The nanowire is represented by a p-n diode, a current generator, a series resistance and a shunt resistance. Adapted with permission from Nano Lett. 2021, 21, 21, 9038–9043 (Paper III). Copyright 2021 American Chemical Society.

## 5.5 Nanowires

Two types of nanowires were investigated in this work, p-doped GaAs nanowires and radially doped p-i-n GaAs solar cell nanowires. They were fabricated through SC-MBE by P. Krogstrup et al. [67]. A p-doped (111) Si substrate was heated to 630 °C and a flux of Ga and $As_4$ was introduced into the chamber. The p-doping was achieved by introducing an additional flux of beryllium during the axial growth of the nanowires [112]. For the solar cell nanowires, the axial growth was followed by a change in growth parameters to promote radial growth. During the radial growth of the wires, a thin intrinsic layer was formed, whereafter an n-doped shell was grown by adding a flux of Si [27]. The total diameter of the nanowires was typically in the range 200-350 nm, and the length in the range 15-25 µm. The thicknesses of the p- i- and n-layers were approximately 100-120 nm, 15 nm and 60-80 nm, respectively. The doping concentration was $3.5e^{19}$ for p-doping and $5e^{18}$ for n-doping, as estimated from planar growth.

# 6. Results and discussion

## 6.1 Microstructure of GaAs nanowires

The microstructure of the nanowires were investigated using TEM imaging and diffraction. The structure of a representative nanowire is shown in Figure 6.1. The high resolution TEM (HRTEM) micrograph and the corresponding electron diffraction pattern in Figure 6.1 (a) and (c) reveal that the crystal structure of the nanowire is ZB. They also show that the nanowire contains TPs, oriented perpendicular to the long axis of the nanowire, and that a native oxide layer with thickness ∼5 nm is present at the nanowire surface. In the diffraction pattern, many diffraction spots appear in pairs. This is a result of the twins and the two spots in a pair correspond to the two sets of twins in the nanowire. The dark field image in Figure 6.1 (b) was produced by choosing only one of the spots in a pair and in (d) the other spot was chosen to form the image. In this way, the distribution of twins and TPs are revealed at a larger scale. It is evident that even though a few TPs are located in close vicinity, most of them are separated by more than 50 nm, and should therefore not have a significant effect on the resistivity of the wire, see section 2.2.

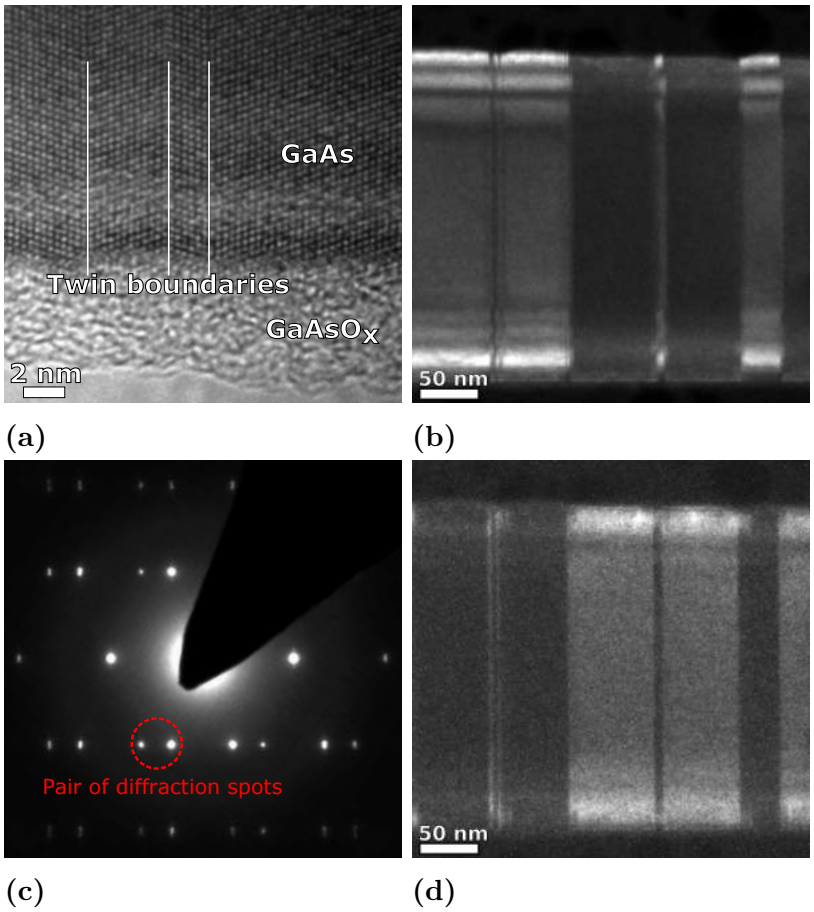


**Figure 6.1:** **(a)** and **(c)**: High resolution TEM image of GaAs nanowire and corresponding diffraction pattern. Twin planes where the crystal orientation changes are visible in the image and show up as pairs of spots in the diffraction pattern. **(b)** and **(d)**: Dark field images recorded at lower magnification showing spatial distribution of twin domains. Dark areas in the upper image are bright in the lower and vice versa, because the two images were generated by choosing one or the other diffraction spot in a pair. The horizontal stripes is a result of sample thickness variation across the nanowire.

## 6.2 Electrical contact

Many individual as-grown nanowires were contacted in the way described in section 5.4 using a movable probe in an in situ FIB-SEM setup, see Figure 6.2, and I-V characteristics were retrieved both under dark and illuminated conditions. A representative result of this type of measurement on a radially p-i-n doped GaAs nanowire is shown in Figure 6.3 (a). The illuminated I-V curve does not follow the superposition principle which is applicable for a high quality solar cell. Instead it is S-shaped around zero bias, reducing both the $I_{SC}$, $V_{OC}$ and FF of the solar cell. This S-shape is due to the formation of a strong Schottky barrier at the semiconductor-metal contact, as discussed in section 4.2.2. For the results to be representative of the intrinsic properties of the nanowires, it is therefore crucial to optimize the electrical contact between the probe and the nanowires.

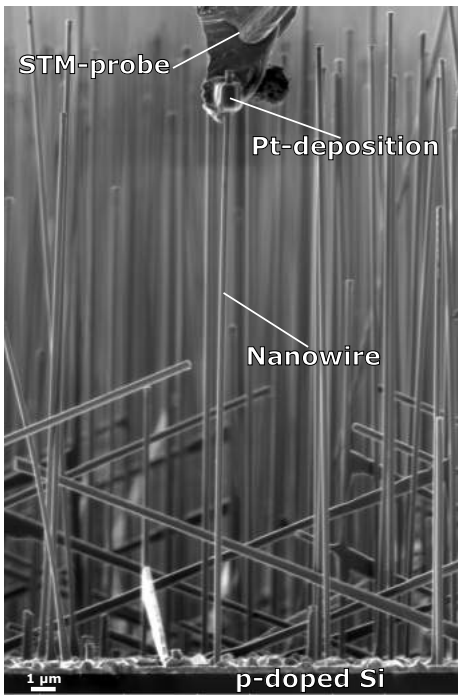


**Figure 6.2:** SEM image of an individually contacted GaAs nanowire.

In order to investigate the quality of the contact on as-grown nanowires, a TEM lamella of a nanowire cross section was prepared using FIB-SEM, see Figure 6.3 (b) and 6.3 (c). From these TEM micrographs, it is clear that there is an approximately 5 nm thick amorphous layer between the crystalline GaAs in the nanowire and the Pt deposited in FIB-SEM. This amorphous layer is a native oxide layer since all the nanowires in this work have been exposed to air. As discussed in section 4.2.1, an insulating layer between the semiconductor and the metal reduces the tunneling probability through the Schottky barrier and can significantly reduce the current. In order to improve the electrical contact, it is therefore important to remove the native oxide layer.

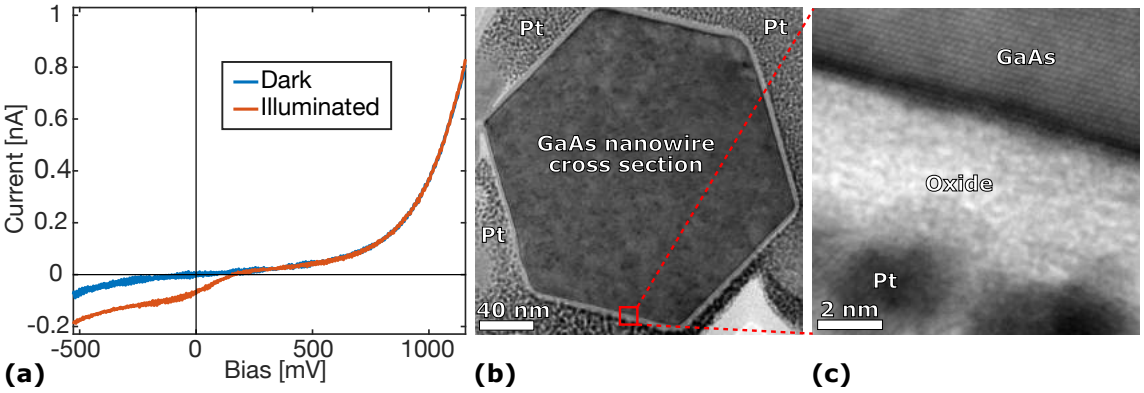


**Figure 6.3:** **(a)** Dark and illuminated I-V characteristics of a nanowire contacted as-grown. The illuminated I-V curve has a kink, indicating a rectifying contact. **(b)** TEM micrograph of a cross-sectional sample of an as-grown nanowire. **(c)** Zoom-in of the area marked with a red square in (b). The Pt and the GaAs are separated by the native oxide layer of the nanowire.

Two different strategies were adopted to remove the oxide layer. The first one was to mill the surface of the nanowire at the contact area, before connecting the probe and the nanowire. This was done using a focused Ga ion beam with an acceleration voltage of 2 kV and a beam current of 27 pA in FIB-SEM. Figure 6.4 (b) shows a TEM micrograph of a cross section of a nanowire of which the surface has been milled. The oxide layer is removed at the milled area, however the nanowire itself has also been affected by the ion beam. By comparing the shape of the cross section to a perfect hexagonal, it is clear that a surface layer of approximately 15 nm has been milled away from the nanowire. However, the thickness of the n-doped shell of the nanowire is approximately 60-80 nm, so the p-i-n junction is not damaged by this treatment. The outermost part of the nanowire that has been exposed to the ion beam has a darker contrast, see Figure 6.4 (c), indicating that this region is structurally different from the rest of the nanowire. This is not surprising since the ion beam can introduce defects or even completely amorphize the sample close to the surface. Implantation of Ga-ions from the FIB can also occur. Figure 6.4 (a) shows the I-V characteristics of a milled nanowire, and there is no S-shape of the illuminated I-V curve. The dark current is also significantly higher than for the unmilled one. Hence, the contact is improved by the milling. The main reason for this is most likely that the insulating oxide layer is removed. However, instead of the oxide layer, there is now a defect-rich or amorphous layer between the crystalline GaAs and the Pt. There may be several reasons why this layer is not as insulating as the oxide. Firstly, the defects may introduce trapped charges and electronic states within the band gap, resulting in an alternative current path. Secondly, the layer may be Ga-rich because of Ga ion implantation which would make it more metallic and thus more conducting than the oxide.

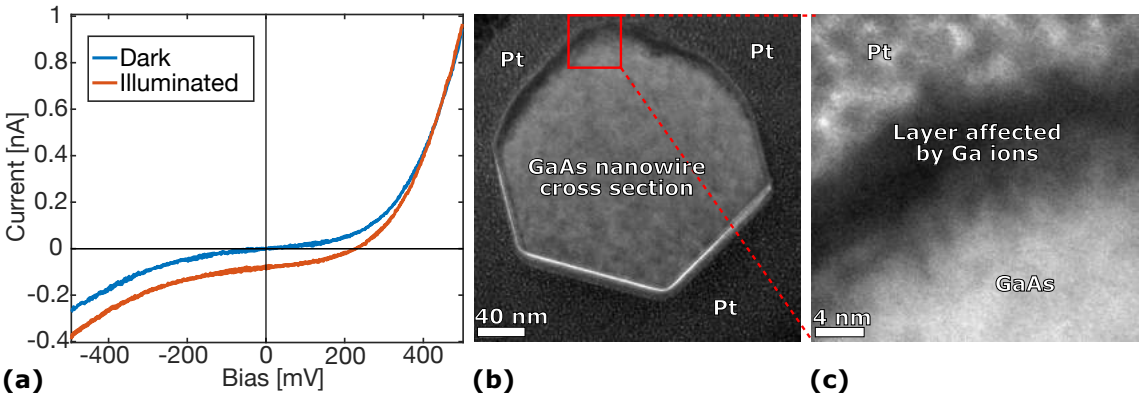


**Figure 6.4:** **(a)** Dark and illuminated I-V characteristics of a nanowire FIB-milled at the contact area. The current is high compared to the as-grown nanowire and the illuminated I-V curve has no kink, indicating a low resistive, non-rectifying contact. **(b)** TEM micrograph of cross sectional sample of a FIB-milled nanowire. Part of the nanowire itself has been milled away. **(c)** Zoom-in of the area highlighted in (b). The oxide layer between the GaAs and the Pt is absent.

The other strategy to improve the electrical contact was to apply Joule heating in order to heat up the contact area until the contact resistance is reduced. In practice this was done by contacting a nanowire and apply a large bias so that a current of around 1-2 $\mu$A passed through the contact. Since the contact is the most resistive part, most heat is generated there. However, at some point the contact resistance will quickly drop and the current will increase significantly. If the current reaches values >5 $\mu$A, there is a risk that the nanowire is damaged. A series resistance of 5 M$\Omega$ was therefore added to the circuit during Joule heating, and the bias was kept below 20 V. Figure 6.5 (a) shows the dark and illuminated I-V characteristics of a single nanowire before and after Joule heating. It is clear that this treatment improves the quality of the contact, since the S-shape disappears and the dark current increases afterwards. It is assumed that the heat disperses the oxide layer and the thickness of the barrier is reduced, increasing the tunneling probability, but it has not yet been experimentally confirmed.

Figure 6.5 (b) shows the I-V characteristics under dark conditions for a large selection of nanowires. Each curve corresponds to a unique wire, either contacted as-grown, FIB-milled or Joule heated. The trend is clear; both FIB-milled and Joule heated contacts generally result in a higher current at a certain applied bias than as-grown contacts.

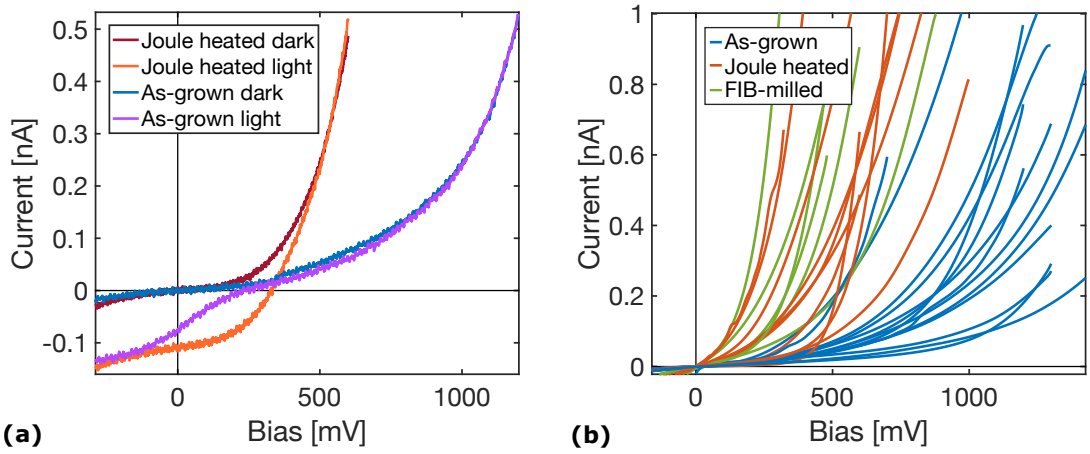


**Figure 6.5:** **(a)** Dark and illuminated I-V characteristics of a single nanowire before and after contact optimization by Joule heating. **(b)** Dark I-V characteristics of a large selection of nanowires that was either contacted as-grown, FIB-milled or Joule heated.

## 6.3 Photovoltaic properties

Using either the FIB-milling or Joule heating process to establish high quality contact, the intrinsic photovoltaic properties of individual GaAs nanowires with radial p-i-n junctions were investigated. The I-V characteristics of two different nanowires during white LED illumination are shown in Figure 6.6 (a). Table 6.1 shows the corresponding photovoltaic parameters. It should be noted that the PCE-values received for single nanowires using our setup cannot be directly compared to PCE-values received from standardized tests on full scale solar cells. One reason is that the waveguiding effect of the nanowires makes the area to be used in the calculation of the total incoming light intensity ambiguous. Another reason is that the the wavelength spectrum of the white LED is not equal to the solar spectrum, see Figure 6.6 (b). Furthermore, the LED-light is incident at an angle of 10-40° relative to the sample normal, as opposed to standardized conditions where the incoming light is parallell to the sample normal. Additionally, part of the incoming light may be blocked by the STM-probe and other nanowires. Therefore, the PCE-values should strictly be used to compare the performance of different individual nanowires mutually.

We see in Table 6.1 that Nanowire 2 has high $V_{OC}$ and $FF$, resulting in a high PCE despite a low $I_{SC}$. Nanowire 1 has lower $V_{OC}$ and $FF$, but significantly higher $I_{SC}$, resulting in the highest PCE. By using the model described in section 5.4 to perform numerical data-fitting of the I-V curves in Figure 6.6, the parameters describing the p-i-n junctions of the wires were extracted, see the three rightmost columns of Table 6.1. The most distinguishing feature is $I_S$, which is significantly lower for Nanowire 2. One probable reason for this is that Nanowire 1 was ∼25 µm long while Nanowire 2 was ∼10 µm long. The area of the p-i-n junction scales with the nanowire length due to its radial geometry, which in turn affects $I_S$, as

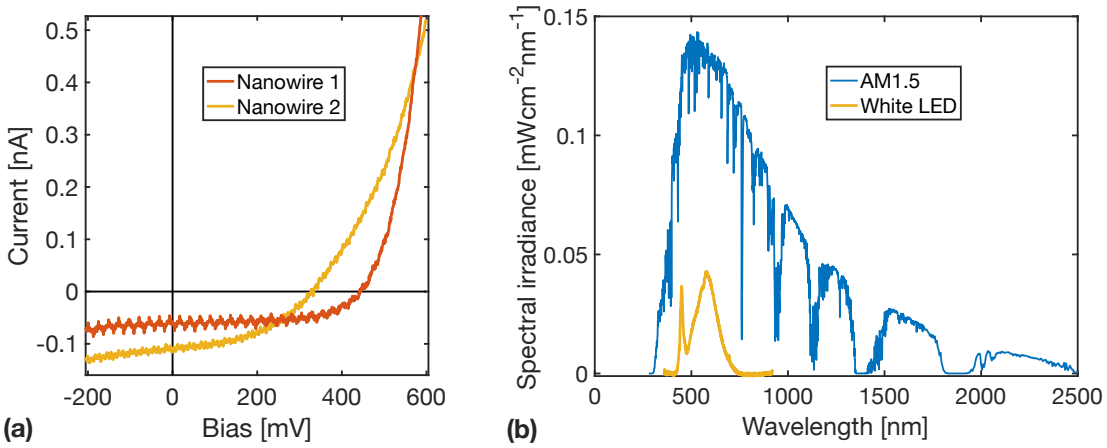


**Figure 6.6:** **(a)** I-V characteristics of two different nanowires during white LED illumination. The periodic noise present for Nanowire 1 stems from the surrounding electrical grid, because the setup was not optimally shielded at the time. **(b)** Comparison between the solar spectrum AM1.5 and the white LED spectrum.

discussed in Section 3.4. The shorter nanowire may therefore have a lower $I_S$ and as a result a higher $V_{OC}$, according to equation 3.4. The shorter nanowire also has a smaller smaller area exposed to the illumination, which may explain the low $I_{SC}$ for Nanowire 2.

**Table 6.1:** Photovoltaic and electrical parameter values

| Nanowire | $I_{SC}$ $[pA]$ | $V_{OC}$ $[mV]$ | $FF$ | $PCE^*$ | $R_{sh}$ $[G\Omega]$ | $I_S$ $[pA]$ | $n$ |
|---|---|---|---|---|---|---|---|
| 1 | 110 | 330 | 0.44 | 10.8% | 40 | 2.5 | 4 |
| 2 | 61 | 442 | 0.59 | 9.7% | 40 | 0.01 | 2.3 |

## 6.4 Strain-induced effects

The strain-induced effects on the electrical and photovoltaic properties of individual nanowires were investigated. The nanowires were exposed to uniaxial tensile or compressive strain by moving the probe either away from or towards the substrate. In many cases, more than 3% tensile strain could be applied before the fracture of the wires. Figure 6.7 shows the result of one such measurement on a p-i-n doped nanowire. This nanowire was FIB-milled to optimize the contact. The amount of strain was calculated by dividing the elongation of the wire by its original length. The elongation and the length was measured from the SEM images shown in 6.7 (a). At each strain level, the I-V characteristics were retrieved, see 6.7 (b). The strain has significant effects on the I-V characteristics. In order to investigate the reversibility of these effects, the nanowire was relaxed and strained once more. The I-V characteristics during the first and the second straining cycle agreed well, showing that the strain-induced effects were indeed reversible. Again, the model in section 5.4 was used for numerical data-fitting of the I-V curves, in order to quantitatively

determine the effect of strain upon the electrical nanowire properties. Figure 6.7 (c) shows that the $I_S$ of the p-i-n junction increases as a function of strain. With $I_S$ being known, equation 3.2 were used to calculate $E_g$ as a function of strain. The result is shown in Figure 6.7 (d). According to this, $E_g$ decreases monotonously with increasing strain, from 1.42 eV at zero strain to around 1.2 eV at 3 % strain.

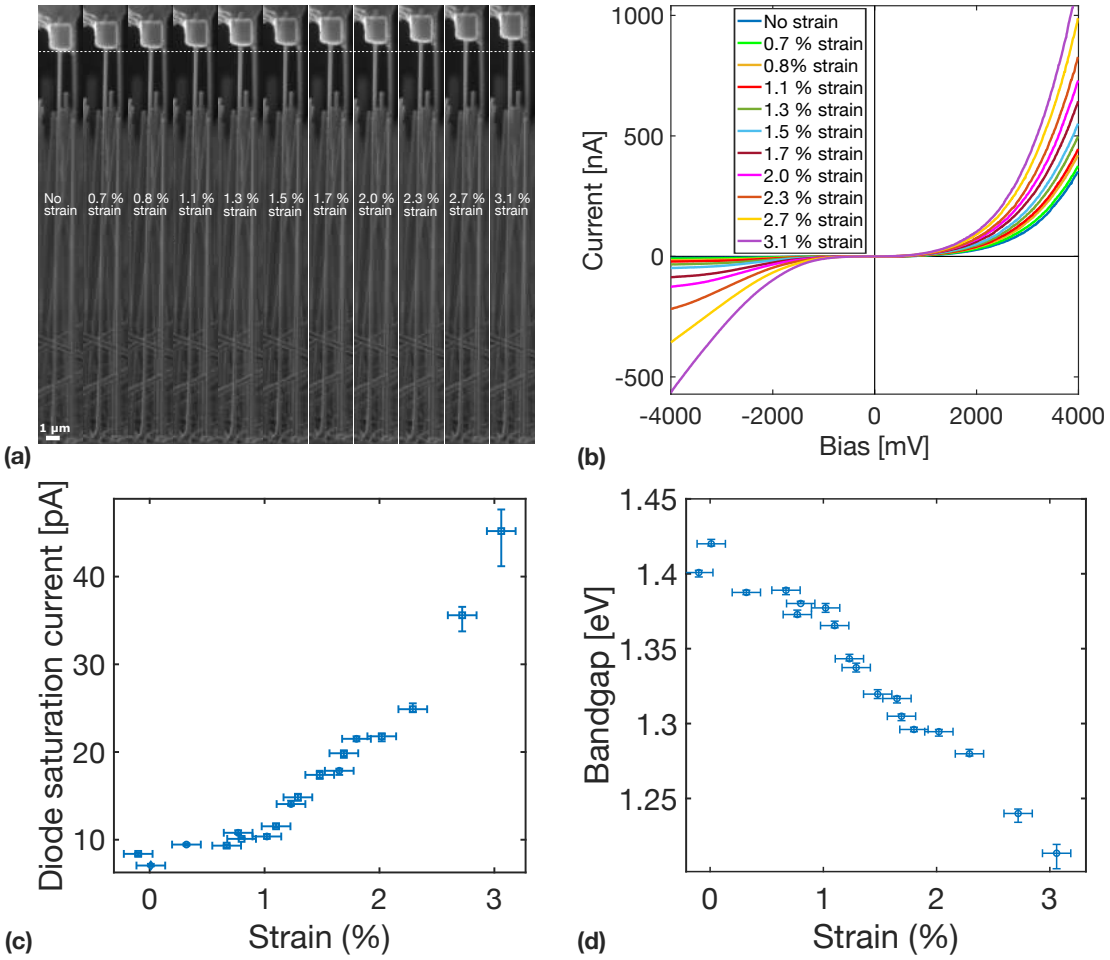


**Figure 6.7:** **(a)** SEM images showing one straining cycle of a single GaAs nanowire with radial p-i-n junction. **(b)** I-V characteristics corresponding to the different straining levels. **(c)** Diode saturation current of the p-i-n junction as a function of strain. **(d)** Band gap energy of the nanowire as a function of strain.

The nanowire resistance, $R_{NW}$, was also affected by the strain. Figure 6.8 shows $R_{NW}$ as a function of strain for 5 different nanowires, two with p-i-n doping and three with only p-doping. The trend for all of the wires is the same: the resistance increases at moderate strain levels, up to around 1-2%, but as the strain increases further, $R_{NW}$ starts to decrease instead. This effect is attributed to the strain-induced energy splitting of the degenerate heavy and light hole bands in GaAs. This splitting causes the average hole effective mass to increase, which in turn increases the resistivity. However, at high strain levels the splitting of the bands is large enough to suppress interband phonon scattering, which in turn decreases the resistivity. For more details

about the band-splitting, see Paper II. Furthermore, the parameters $\phi_B$, $R_{sh}$ and $R_C$, all decreased with increasing strain, for more details see Paper III.

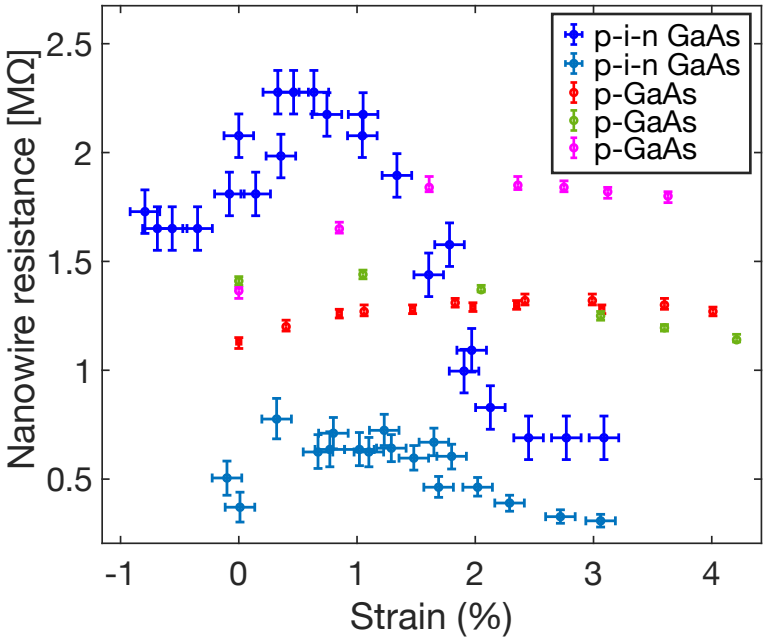


**Figure 6.8:** Nanowire resistance as a function of strain for five different nanowires, two with radial p-i-n junctions and three p-doped.

The strain-induced effects of the photovoltaic properties were also investigated. Two nanowires were illuminated with near-infrared (NIR) LED and one with a green LED, see Figure 6.9 (a) for the different LED wavelength spectra. The corresponding I-V characteristics are shown in Figure 6.9 (b-d).

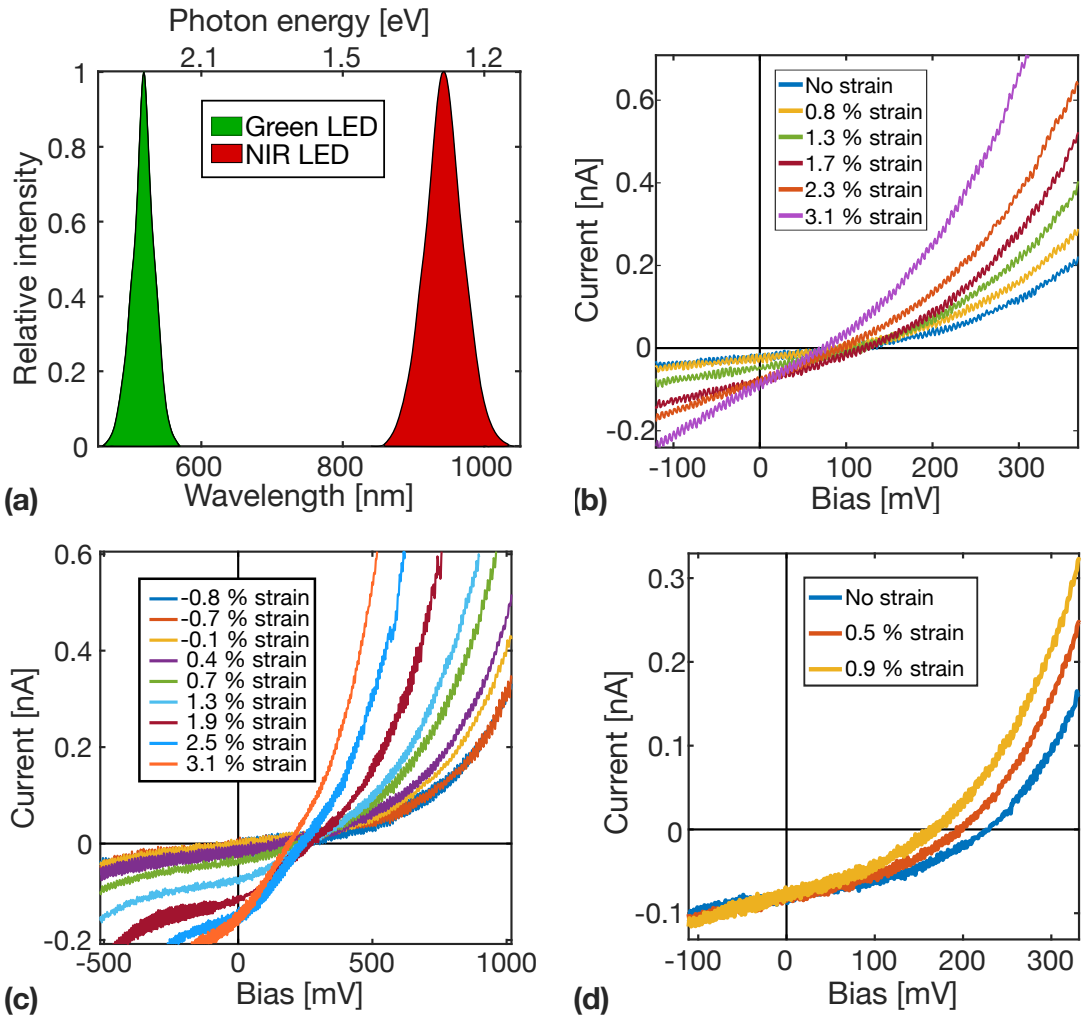


**Figure 6.9:** **(a)** Normalized light intensity as a function of wavelength for the green LED and the NIR LED that were used to illuminate the nanowires during straining. **(b)** I-V characteristics of a single nanowire during NIR LED illumination at different strain levels. **(c)** I-V characteristics of another single nanowire during NIR LED illumination at different strain levels. **(d)** I-V characteristics of a third single nanowire during green LED illumination at different strain levels.

The parameters $I_{SC}$, $V_{OC}$, $FF$ and $PCE$, describing the photovoltaic performance of the three nanowires, are plotted as a function of strain in Figure 6.10 (a-d), respectively. In the case of NIR LED illumination, $I_{SC}$ is small at no strain and increases with increasing strain until it reaches a plateau, see Figure 6.10 (a). For green LED illumination though, it starts at a high value and is not significantly influenced by the strain. This may be explained by examining the wavelength spectra for the two different LED:s. For the green LED, all the photons have energies well above 1.42 eV which is the band gap energy of GaAs. These photons will therefore be absorbed regardless of the strain applied. For the NIR LED though, most photons have energies below 1.42 eV and will not get absorbed in an unstrained nanowire. When the nanowire is strained though, the band gap decreases and the NIR photons can get absorbed. The increase in $I_{SC}$ is thus consistent with the

calculated shift in $E_g$ due to strain shown in Figure 6.7 (c). The plateau is reached when $E_g$ has shifted outside of the NIR LED spectrum. Had this spectrum been wider, $I_{SC}$ would probably have continued to increase all the way up to 3 % strain. Moving on to Figure 6.10 (b), we see that during NIR illumination, $V_{OC}$ increases up to 1.5-2 % strain, but decreases at higher strain levels. This effect can be explained by considering equation 3.4, that states that $V_{OC}$ is directly proportional to $I_{SC}$, and inversely proportional to $I_s$. Since $I_{SC}$ increases significantly between 0 and 2 % strain, $V_{OC}$ also increases. Above 2 % strain though, $I_{SC}$ reaches a plateau, and the reduction in $V_{OC}$ is caused by an increase in $I_s$. In the case of green LED illumination though, $I_{SC}$ remains almost constant while $I_s$ increases during the straining, causing a monotonous reduction in $V_{OC}$. $FF$ follows the same trend as $V_{OC}$ for the three respective nanowires. Finally, considering the PCE as a function of strain shown in Figure 6.10 (d), we see that during NIR illumination it increases up to a certain point beyond which it starts to decrease again. Observe that the decline in PCE at high strain is mainly associated with the narrow spectrum of the NIR LED. During green LED illumination, the PCE instead declines steadily with increasing strain. These results are in line with the detailed balanced theory discussed in section 3.3, which boils down to the fact that for a single band gap solar cell, the optimal band gap energy is a compromise between absorbing as many photons as possible, and utilizing as much energy of each absorbed photon as possible.

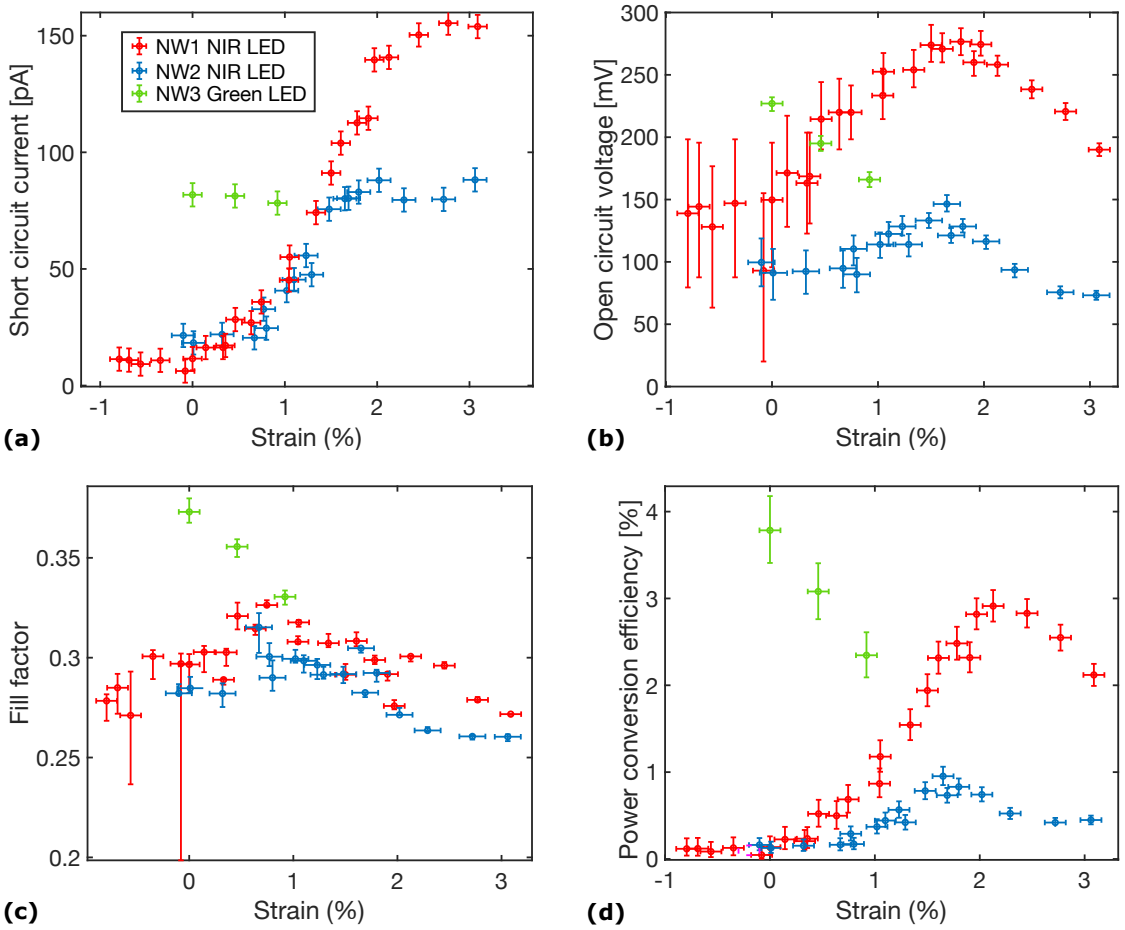


**Figure 6.10:** The photovoltaic parameters $I_{SC}$ **(a)**, $V_{OC}$ **(b)**, $FF$ **(c)** and PCE **(d)** as a function of strain for three different nanowires. Nanowire 1 and 2 were illuminated with a NIR LED and nanowire were illuminated with a green LED.

## 6.5 EBIC mapping

In order to investigate the charge-separation ability locally within the nanowires, and the effect of strain on it, EBIC mapping of several nanowires was performed. The result of one such measurement is shown in Figure 6.11. This nanowire was contacted as-grown, and the contact was placed a few µm below the tip of the nanowire in order to have a region that would remain unstrained throughout the experiment. Figure 6.11 (a) and (b) shows an EBIC map and the corresponding SEM image of the nanowire without any strain applied. The EBIC map shows that the whole nanowire is active, meaning that it separates the electron-hole pairs generated by the electron beam, giving rise to an EBIC signal. This confirms that there exists a radial p-i-n junction throughout the whole nanowire, just as expected from the nanowire growth. Figure 6.11 (c) shows the EBIC line profile, meaning the EBIC signal value at the center of the nanowire along its length axis, both in the strained and the relaxed state. First of all, we notice that the EBIC signal increases towards the bottom of the nanowire, except for at the contact were the beam is

partly blocked by the deposited Pt. This feature could be due to redistribution of the charge carriers into the junction during their transport to the contacts, leading to recombination. The higher the resistance of the transport path is, the more redistribution and recombination occurs [113]. The holes and the electrons have different transport paths. The holes go through the p-doped core of the wire and are collected through the substrate, while the electrons go through the n-doped shell and are collected through the STM-probe. Since the hole mobility is lower than the electron mobility for GaAs, we expect less redistribution (and higher EBIC signal) when the hole transport path is shorter, i.e when the electron beam is closer to the bottom of the nanowire. Secondly, we see that as strain is applied to the nanowire, the EBIC signal decreases. When the strain is relaxed, the EBIC signal goes back to the original. The important thing to notice here though is that the EBIC signal decreases everywhere in the nanowire, even in the unstrained part. This indicates that it is most likely a contact effect, and not related to the intrinsic properties of the nanowire.

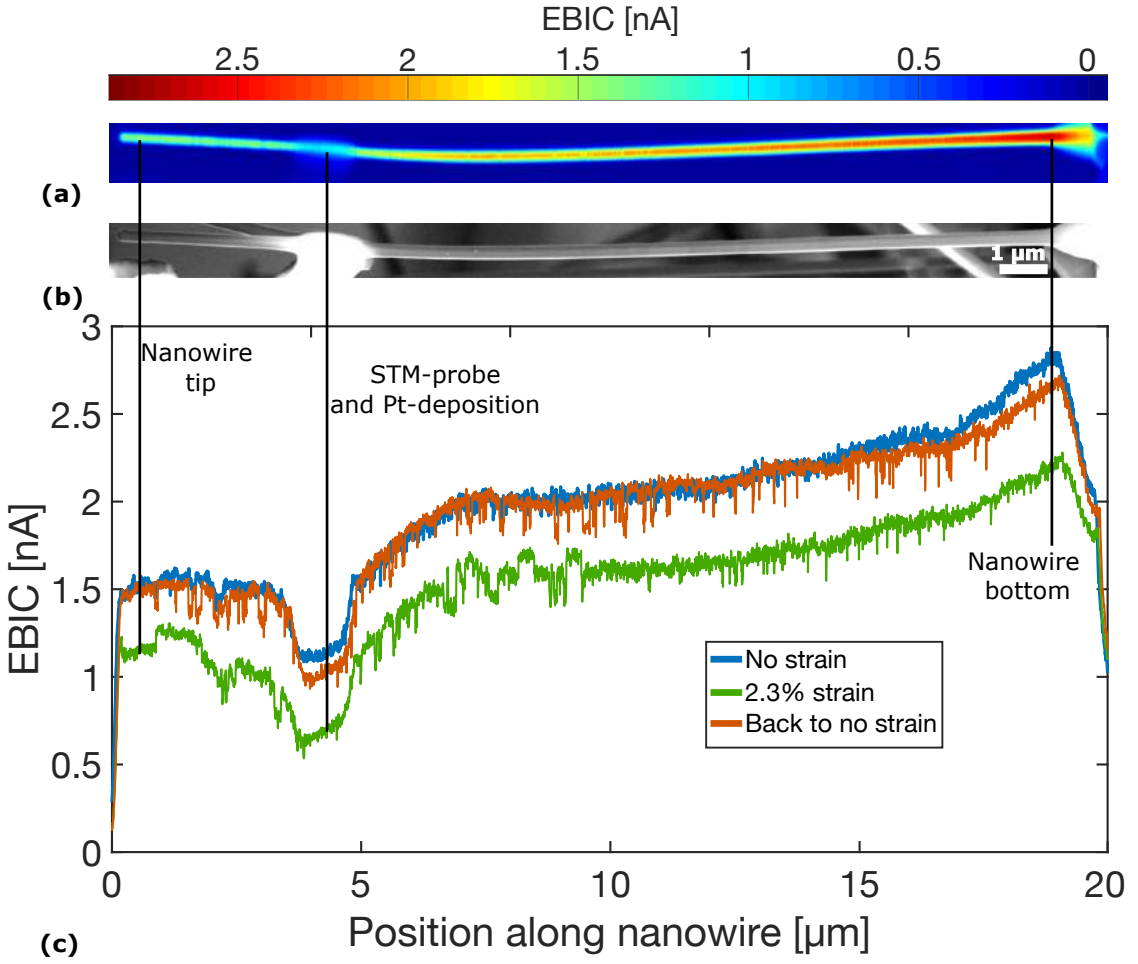


**Figure 6.11:** EBIC-mapping of strained nanowire contacted as-grown. **(a)** EBIC map of the nanowire in the relaxed state. **(b)** SEM image of the nanowire in the relaxed state. **(c)** EBIC line profiles of the nanowire in relaxed and strained states.

Another measurement was performed where the nanowire was bent by pushing the STM-probe towards the substrate, see Figure 6.12 (a). This nanowire was also contacted as-grown, a few µm below the tip. The EBIC line profiles at the different bending-stages are shown in 6.12 (b). The bumps that appear at approximately 12 µm and 20 µm below the tip are artefacts arising due to the fact that the nanowire did not bend perfectly in-plane. This causes the interaction volume to increase at the positions of out-of-plane bending, since the nanowire surface is tilted with respect to the incoming beam there. More charge carriers are thus generated there and a stronger EBIC signal is measured. Again, the important thing to notice is that the EBIC signal changes even in the unstrained part, but this time it increases. These measurements therefore indicates that, when the nanowires are contacted as-grown, the contact limits the EBIC current, and compressive strain improves the contact while tensile strain impairs it.

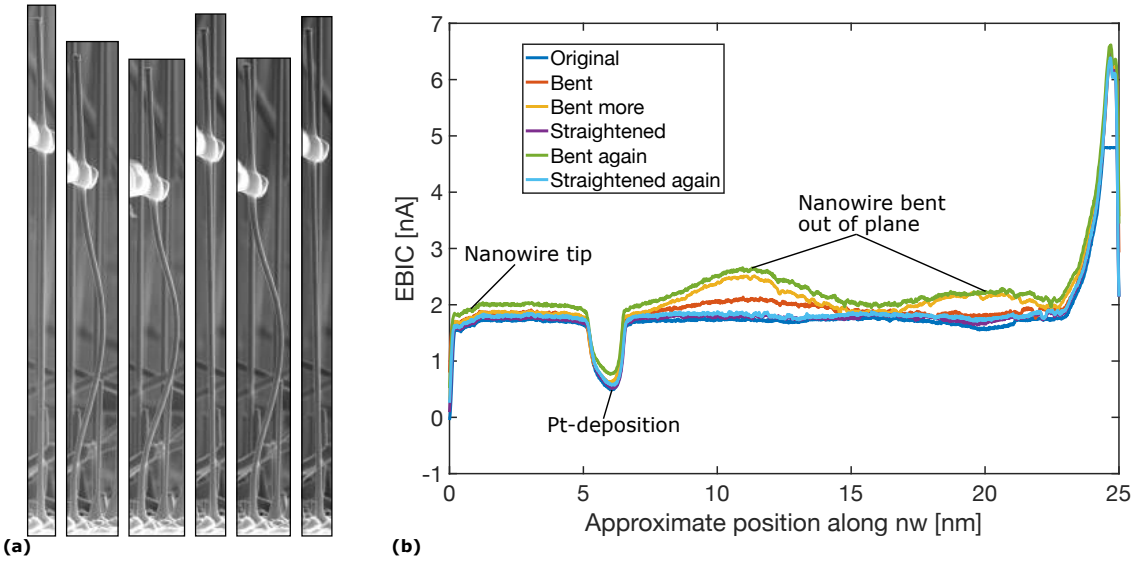


**Figure 6.12:** EBIC measurements on bent, as-grown nanowire. **(a)** SEM images of the different bending stages of the nanowire. **(b)** Corresponding EBIC line profiles. The bumps are artefacts caused by out-of-plane bending.

In order to eliminate the contact effects, a third measurement was performed on a FIB-milled nanowire. An SEM image of the nanowire in the relaxed state and the corresponfing EBIC map are shown in Figure 6.13 (a) and (b), respectively. The EBIC profiles (Figure 6.13 (c)) shows that tensile strain up to 0.9 % does not affect the charge separation ability of the nanowire.

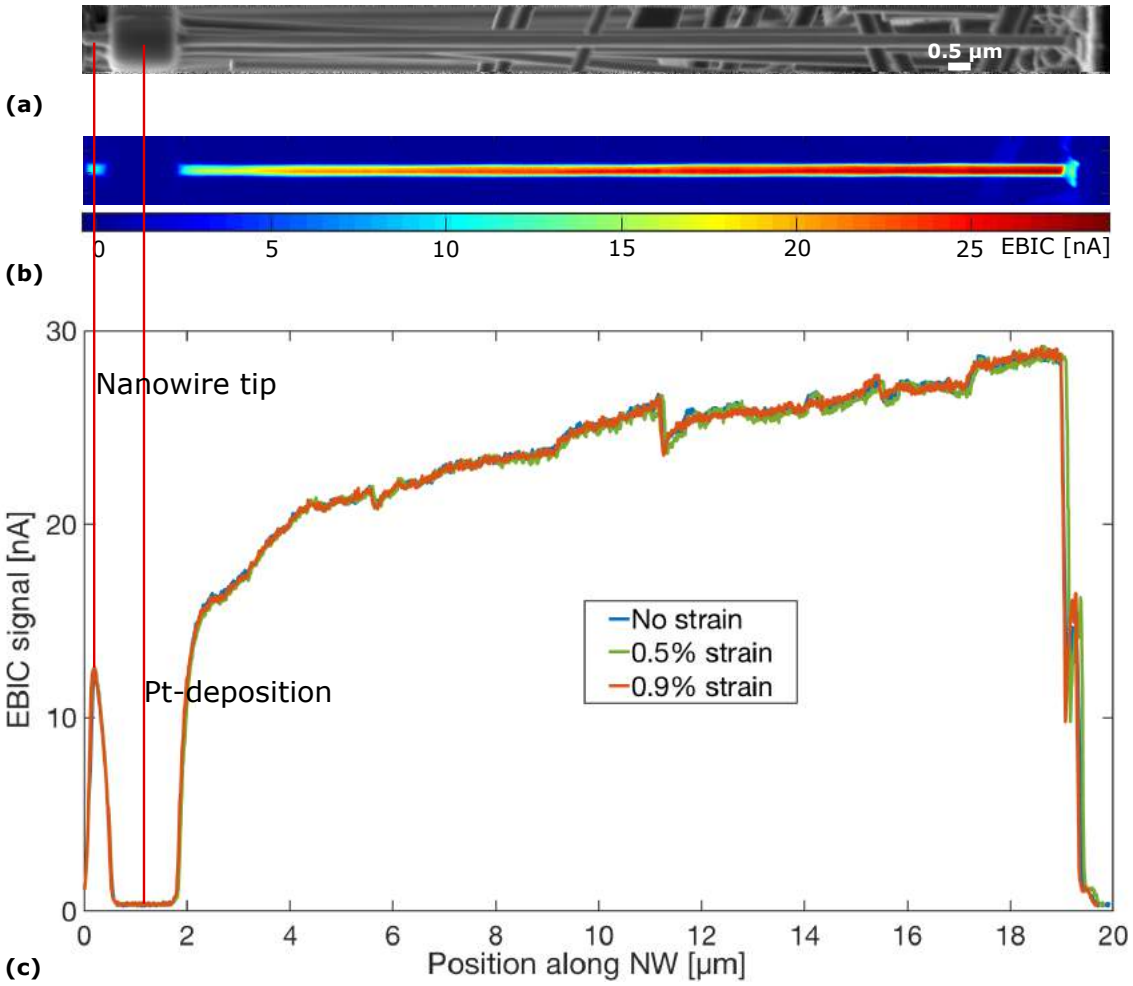


**Figure 6.13:** EBIC mapping of a FIB-milled nanowire. **(a)** SEM image of the nanowire in the relaxed state. **(b)** Corresponding EBIC map. **(c)** EBIC line profiles at different strain levels. The EBIC signal is not affected by the strain when the contact has been optimized.

# 7. Conclusions and outlook

In this work, individual GaAs nanowires were investigated using an in situ STM-SEM setup. It was found that the electrical contact between the STM-probe and the nanowire had a strong impact on the I-V characteristics. Two different procedures, FIB-milling and Joule heating, were successfully used to improve the quality of the contact. With the electrical contact being optimized, the photovoltaic properties of the nanowires were investigated. The best performing nanowire had an apparent efficiency of 10.8%, however this does not directly correspond to a full-scale nanowire solar cell efficiency. It is interesting to note that the length of radially doped nanowires affects the $V_{OC}$. For optimized performance, the nanowires should therefore be just long enough to absorb the incoming light.

Furthermore, elastic strain was shown to have a significant impact on the I-V characteristics of the nanowires. Analysis of the I-V curves showed that $E_g$ decreased with increasing strain, with a maximum shift of 0.2 eV at 3% strain. This resulted in a red-shift in the nanowire absorption range, and the photocurrent during NIR LED illumination was significantly enhanced by strain. This implicates that it would be possible to use elastic strain engineering to improve the performance of nanowire solar cells. The natural next step would be to find a way to introduce a strain gradient in the nanowires, creating a continuous decrease in $E_g$ going from top to bottom. In this way, the Shockley-Queisser limit could be overcome, just as in a multijunction solar cell, but without the need to form material heterostructures. Reverse-tapered nanowires or surface passivation with varying thickness could be two possible ways to realize strain-gradients.

The experimental method that was developed is generic and could be used to study other material structures of interest in the future. The theoretical model that was used to analyze the I-V characteristics and separate the intrinsic nanowire properties from contact-effects, could be modified to describe other material systems. 2D-materials is one example that would be interesting to investigate using the technique.

# Bibliography

[1] N. P. Dasgupta, J. Sun, C. Liu, S. Brittman, S. C. Andrews, J. Lim, H. Gao, R. Yan, and P. Yang, "25th anniversary article: Semiconductor nanowires - Synthesis, characterization, and applications," *Advanced Materials*, vol. 26, no. 14, pp. 2137–2184, 2014.

[2] J. Goldberger, A. I. Hochbaum, R. Fan, and P. Yang, "Silicon vertically integrated nanowire field effect transistors," *Nano Letters*, vol. 6, no. 5, pp. 973–977, 2006.

[3] M. Law, D. J. Sirbuly, J. C. Johnson, J. Goldberger, R. J. Saykally, and P. Yang, "Nanoribbon waveguides for subwavelength photonics integration," *Science*, vol. 305, no. 5688, pp. 1269–1273, 2004.

[4] M. H. Huang, S. Mao, H. Feick, H. Yan, Y. Wu, H. Kind, E. Weber, R. Russo, and P. Yang, "Room-temperature ultraviolet nanowire nanolasers," *Science*, vol. 292, no. 5523, pp. 1897–1899, 2001.

[5] C. Hahn, Z. Zhang, A. Fu, C. H. Wu, Y. J. Hwang, D. J. Gargas, and P. Yang, "Epitaxial growth of InGaN nanowire arrays for light emitting diodes," *ACS Nano*, vol. 5, no. 5, pp. 3970–3976, 2011.

[6] J. Li, Z. Shan, and E. Ma, "Elastic strain engineering for unprecedented materials properties," *MRS Bulletin*, vol. 39, no. 02, pp. 108–114, 2014.

[7] G. Signorello, E. Lörtscher, P. A. Khomyakov, S. Karg, D. L. Dheeraj, B. Gotsmann, H. Weman, and H. Riel, "Inducing a direct-to-pseudodirect bandgap transition in wurtzite GaAs nanowires with uniaxial stress," *Nature Communications*, vol. 5, no. 7491, 2014.

[8] G. Signorello, S. Karg, M. T. Björk, B. Gotsmann, and H. Riel, "Tuning the light emission from GaAs nanowires over 290 meV with uniaxial strain," *Nano Letters*, vol. 13, no. 3, pp. 917–924, 2013.

[9] R. He and P. Yang, "Giant piezoresistance effect in silicon nanowires," *Nature Nanotechnology*, vol. 1, no. 1, pp. 42–46, 2006.

[10] D. Van Dam, N. J. Van Hoof, Y. Cui, P. J. Van Veldhoven, E. P. Bakkers, J. Gómez Rivas, and J. E. Haverkort, "High-Efficiency Nanowire Solar Cells with Omnidirectionally Enhanced Absorption Due to Self-Aligned Indium-Tin-Oxide Mie Scatterers," *ACS Nano*, vol. 10, no. 12, pp. 11 414–11 419, 2016.

[11] I. Vurgaftman, J. R. Meyer, and L. R. Ram-Mohan, "Band parameters for III-V compound semiconductors and their alloys," *Journal of Applied Physics*, vol. 89, no. 11 I, pp. 5815–5875, 2001.

[12] R. S. Wagner and W. C. Ellis, "Vapor-liquid-solid mechanism of single crystal growth," *Applied Physics Letters*, vol. 4, no. 5, pp. 89–90, 1964.

[13] T. Hamano, H. Hirayama, and Y. Aoyagi, "New technique for fabrication of two-dimensional photonic bandgap crystals by selective epitaxy," *Japanese Journal of Applied Physics, Part 2: Letters*, vol. 36, no. 3 A, 1997.

[14] N. Dhindsa, A. Chia, J. Boulanger, I. Khodadad, R. LaPierre, and S. S. Saini, "Highly ordered vertical GaAs nanowire arrays with dry etching and their optical properties," *Nanotechnology*, vol. 25, no. 30, 305303(11pp), 2014.

[15] N. Dhindsa and S. S. Saini, "Top-down fabricated tapered GaAs nanowires with sacrificial etching of the mask," *Nanotechnology*, vol. 28, no. 23, 2017.

[16] E. Barrigón, M. Heurlin, Z. Bi, B. Monemar, and L. Samuelson, "Synthesis and Applications of III-V Nanowires," *Chemical Reviews*, vol. 119, no. 15, pp. 9170–9220, 2019.

[17] J. C. Harmand, G. Patriarche, F. Glas, F. Panciera, I. Florea, J. L. Maurice, L. Travers, and Y. Ollivier, "Atomic Step Flow on a Nanofacet," *Physical Review Letters*, vol. 121, no. 16, p. 166 101, 2018.

[18] D. E. Perea, J. E. Allen, S. J. May, B. W. Wessels, D. N. Seidman, and L. J. Lauhon, "Three-dimensional nanoscale composition mapping of semiconductor nanowires," *Nano Letters*, vol. 6, no. 2, pp. 181–185, 2006.

[19] J. E. Allen, E. R. Hemesath, D. E. Perea, J. L. Lensch-Falk, Z. Y. Li, F. Yin, M. H. Gass, P. Wang, A. L. Bleloch, R. E. Palmer, and L. J. Lauhon, "High-resolution detection of Au catalyst atoms in Si nanowires," *Nature Nanotechnology*, vol. 3, no. 3, pp. 168–173, 2008.

[20] J. P. Boulanger, A. C. Chia, B. Wood, S. Yazdi, T. Kasama, M. Aagesen, and R. R. LaPierre, "Characterization of a Ga-Assisted GaAs Nanowire Array Solar Cell on Si Substrate," *IEEE Journal of Photovoltaics*, vol. 6, no. 3, pp. 661–667, 2016.

[21] K. Ikejiri, J. Noborisaka, S. Hara, J. Motohisa, and T. Fukui, "Mechanism of catalyst-free growth of GaAs nanowires by selective area MOVPE," *Journal of Crystal Growth*, vol. 298, no. SPEC. ISS, pp. 616–619, 2007.

[22] S. Franchi, *Molecular beam epitaxy: fundamentals, historical background and future prospects*. Elsevier, 2013, pp. 1–46.

[23] P. Krogstrup, R. Popovitz-Biro, E. Johnson, M. H. Madsen, J. Nygård, and H. Shtrikman, "Structural phase control in self-catalyzed growth of GaAs nanowires on silicon (111)," *Nano Letters*, vol. 10, no. 11, pp. 4475–4482, 2010.

[24] E. Uccelli, J. Arbiol, C. Magen, P. Krogstrup, E. Russo-Averchi, M. Heiss, G. Mugny, F. Morier-Genoud, J. Nygård, J. R. Morante, and A. Fontcuberta I Morral, "Three-dimensional multiple-order twinning of self-catalyzed GaAs nanowires on Si substrates," *Nano Letters*, vol. 11, no. 9, pp. 3827–3832, 2011.

[25] S. Plissard, G. Larrieu, X. Wallart, and P. Caroff, "High yield of self-catalyzed GaAs nanowire arrays grown on silicon via gallium droplet positioning," *Nanotechnology*, vol. 22, no. 27, 2011.

[26] J. Vukajlovic-Plestina, W. Kim, L. Ghisalberti, G. Varnavides, G. Tütüncuoglu, H. Potts, M. Friedl, L. Güniat, W. C. Carter, V. G. Dubrovskii, and A. Fontcuberta i Morral, "Fundamental aspects to localize self-catalyzed III-V nanowires on silicon," *Nature Communications*, vol. 10, no. 1, 2019.

[27] C. Colombo, M. Heiß, M. Grätzel, and A. Fontcuberta I Morral, "Gallium arsenide p-i-n radial structures for photovoltaic applications," *Applied Physics Letters*, vol. 94, no. 17, 2009.

[28] Z. Li, H. H. Tan, C. Jagadish, and L. Fu, "III–V Semiconductor Single Nanowire Solar Cells: A Review," *Advanced Materials Technologies*, vol. 3, no. 9, pp. 1–12, 2018.

[29] T. Ito, "Simple criterion for wurtzite-zinc-blende polytypism in semiconductors," *Japanese Journal of Applied Physics, Part 2: Letters*, vol. 37, no. 10 SUPPL. B, pp. 9–13, 1998.

[30] P. Caroff, J. Bolinsson, and J. Johansson, "Crystal phases in III-V nanowires: From random toward engineered polytypism," *IEEE Journal on Selected Topics in Quantum Electronics*, vol. 17, no. 4, pp. 829–846, 2011.

[31] D. Jacobsson, F. Panciera, J. Tersoff, M. C. Reuter, S. Lehmann, S. Hofmann, K. A. Dick, and F. M. Ross, "Interface dynamics and crystal phase switching in GaAs nanowires," *Nature*, vol. 531, no. 7594, pp. 317–322, 2016.

[32] N. Akopian, G. Patriarche, L. Liu, J. C. Harmand, and V. Zwiller, "Crystal phase quantum dots," *Nano Letters*, vol. 10, no. 4, pp. 1198–1201, 2010.

[33] X. Qian, M. Kawai, H. Goto, and J. Li, "Effect of twin boundaries and structural polytypes on electron transport in GaAs," *Computational Materials Science*, vol. 108, pp. 258–263, 2015.

[34] K. Shimamura, Z. Yuan, F. Shimojo, and A. Nakano, "Effects of twins on the electronic properties of GaAs," *Applied Physics Letters*, vol. 103, no. 2, pp. 1–5, 2013.

[35] W. Shockley and W. T. Read, "Statistics of the recombinations of holes and electrons," *Physical Review*, vol. 87, no. 5, pp. 835–842, 1952.

[36] S. E. Thompson, G. Sun, Y. S. Choi, and T. Nishida, "Uniaxial-process-induced Strained-Si: Extending the CMOS roadmap," *IEEE Transactions on Electron Devices*, vol. 53, no. 5, pp. 1010–1020, 2006.

[37] M. Soutsos and P. Domone, *Construction Materials : Their Nature and Behaviour, Fifth Edition*. Taylor & Francis Group, 2017.

[38] T. Zhu and J. Li, "Ultra-strength materials," *Progress in Materials Science*, vol. 55, no. 7, pp. 710–757, 2010.

[39] P. A. Gabrys, S. E. Seo, M. X. Wang, E. Oh, R. J. Macfarlane, and C. A. Mirkin, "Lattice Mismatch in Crystalline Nanoparticle Thin Films," *Nano Letters*, vol. 18, no. 1, pp. 579–585, 2018.

[40] H. Zhang, J. Tersoff, S. Xu, H. Chen, Q. Zhang, K. Zhang, Y. Yang, C. S. Lee, K. N. Tu, J. Li, and Y. Lu, "Approaching the ideal elastic strain limit in silicon nanowires," *Science Advances*, vol. 2, no. 8, pp. 2–10, 2016.

[41] L. Zeng, C. Gammer, B. Ozdol, T. Nordqvist, J. Nygård, P. Krogstrup, A. M. Minor, W. Jäger, and E. Olsson, "Correlation between Electrical Transport and Nanoscale Strain in InAs/In 0.6 Ga 0.4 As Core-Shell Nanowires," *Nano Letters*, vol. 18, no. 8, pp. 4949–4956, 2018.

[42] G. Signorello, S. Sant, N. Bologna, M. Schraff, U. Drechsler, H. Schmid, S. Wirths, M. D. Rossell, A. Schenk, and H. Riel, "Manipulating Surface States of III-V Nanowires with Uniaxial Stress," *Nano Letters*, vol. 17, no. 5, pp. 2816–2824, 2017.

[43] L. Zeng, T. Kanne, J. Nygård, P. Krogstrup, W. Jäger, and E. Olsson, "The Effect of Bending Deformation on Charge Transport and Electron Effective Mass of p-doped GaAs Nanowires," *Physica Status Solidi - Rapid Research Letters*, vol. 13, no. 8, pp. 1–8, 2019.

[44] L. Balaghi, G. Bussone, R. Grifone, R. Hübner, J. Grenzer, M. Ghorbani-Asl, A. V. Krasheninnikov, H. Schneider, M. Helm, and E. Dimakis, "Widely tunable GaAs bandgap via strain engineering in core/shell nanowires with large lattice mismatch," *Nature Communications*, vol. 10, no. 1, pp. 1–10, 2019.

[45] S. Dimitrijev, *Principles of Semiconductor Devices (2nd Edition)*. Oxford University Press, 2012.

[46] P. Würfel and U. Würfel, *Physics of Solar Cells: From Basic Principles to Advanced Concepts, Second, Updated and Expanded Edition*. Wiley-VCH, 2009.

[47] A. Keppens, W. R. Ryckaert, G. Deconinck, and P. Hanselaer, "High power light-emitting diode junction temperature determination from current-voltage characteristics," *Journal of Applied Physics*, vol. 104, no. 9, 2008.

[48] A. J. Sangster, *Electromagnetic Foundations of Solar Radiation Collection: A Technology for Sustainability*. 2014, vol. 194.

[49] O. D. Miller, E. Yablonovitch, and S. R. Kurtz, "Strong internal and external luminescence as solar cells approach the shockley–queisser limit," *IEEE Journal of Photovoltaics*, vol. 2, no. 3, pp. 303–311, 2012.

[50] J. M. Shah, Y. L. Li, T. Gessmann, and E. F. Schubert, "Experimental analysis and theoretical model for anomalously high ideality factors (n>2.0) in AlGaN/GaN p-n junction diodes," *Journal of Applied Physics*, vol. 94, no. 4, pp. 2627–2630, 2003.

[51] *Reference air mass 1.5 spectra*, May 2022. [Online]. Available: `https://www.nrel.gov/grid/solar-resource/spectra-am1.5.html`.

[52] S. Rühle, "Tabulated values of the Shockley-Queisser limit for single junction solar cells," *Solar Energy*, vol. 130, pp. 139–147, 2016.

[53] W. Shockley and H. J. Queisser, "Detailed balance limit of efficiency of p-n junction solar cells," *Journal of Applied Physics*, vol. 32, no. 3, pp. 510–519, 1961. arXiv: `9809069v1 [arXiv:gr-qc]`.

[54] R. M. France, J. F. Geisz, T. Song, W. Olavarria, M. Young, A. Kibbler, and M. A. Steiner, "Triple-junction solar cells with 39.5% terrestrial and 34.2% space efficiency enabled by thick quantum well superlattices," *Joule*, vol. 6, no. 5, pp. 1121–1135, 2022.

[55] M. A. Green, E. D. Dunlop, J. Hohl-Ebinger, M. Yoshita, N. Kopidakis, K. Bothe, D. Hinken, M. Rauer, and X. Hao, "Solar cell efficiency tables (Version 60)," *Progress in Photovoltaics: Research and Applications*, vol. 30, no. 7, pp. 687–701, 2022.

[56] J. Li, A. Aierken, Y. Liu, Y. Zhuang, X. Yang, J. H. Mo, R. K. Fan, Q. Y. Chen, S. Y. Zhang, Y. M. Huang, and Q. Zhang, "A Brief Review of High Efficiency III-V Solar Cells for Space Application," *Frontiers in Physics*, vol. 8, no. February, pp. 1–15, 2021.

[57] *Best research-cell efficiency chart*, Oct. 2022. [Online]. Available: `https://www.nrel.gov/pv/cell-efficiency.html`.

[58] Y. Cui, J. Wang, S. R. Plissard, A. Cavalli, T. T. Vu, R. P. Van Veldhoven, L. Gao, M. Trainor, M. A. Verheijen, J. E. Haverkort, and E. P. Bakkers, "Efficiency enhancement of InP nanowire solar cells by surface cleaning," *Nano Letters*, vol. 13, no. 9, pp. 4113–4117, 2013.

[59] Q. Gao, Z. Li, L. Li, K. Vora, Z. Li, A. Alabadla, F. Wang, Y. Guo, K. Peng, Y. C. Wenas, S. Mokkapati, F. Karouta, H. H. Tan, C. Jagadish, and L. Fu, "Axial p-n junction design and characterization for InP nanowire array solar cells," *Progress in Photovoltaics: Research and Applications*, vol. 27, no. 3, pp. 237–244, 2019.

[60] I. Aberg, G. Vescovi, D. Asoli, U. Naseem, J. P. Gilboy, C. Sundvall, A. Dahlgren, K. E. Svensson, N. Anttu, M. T. Bjork, and L. Samuelson, "A GaAs nanowire array solar cell with 15.3% efficiency at 1 sun," *IEEE Journal of Photovoltaics*, vol. 6, no. 1, pp. 185–190, 2016.

[61] G. Mariani, Z. Zhou, A. Scofield, and D. L. Huffaker, "Direct-bandgap epitaxial core-multishell nanopillar photovoltaics featuring subwavelength optical concentrators," *Nano Letters*, vol. 13, no. 4, pp. 1632–1637, 2013.

[62] G. Mariani, P. S. Wong, A. M. Katzenmeyer, F. Léonard, J. Shapiro, and D. L. Huffaker, "Patterned radial GaAs nanopillar solar cells," *Nano Letters*, vol. 11, no. 6, pp. 2490–2494, 2011.

[63] Y. Hu, R. R. Lapierre, M. Li, K. Chen, and J. J. He, "Optical characteristics of GaAs nanowire solar cells," *Journal of Applied Physics*, vol. 112, no. 10, 2012.

[64] C. Lin and M. L. Povinelli, "The effect of plasmonic particles on solar absorption in vertically aligned silicon nanowire arrays," *Applied Physics Letters*, vol. 97, no. 7, 2010.

[65] M. Yao, N. Huang, S. Cong, C. Y. Chi, M. A. Seyedi, Y. T. Lin, Y. Cao, M. L. Povinelli, P. D. Dapkus, and C. Zhou, "GaAs nanowire array solar cells with axial p-i-n junctions," *Nano Letters*, vol. 14, no. 6, pp. 3293–3303, 2014.

[66] L. Hrachowina, Y. Zhang, A. Saxena, G. Siefer, E. Barrigon, and M. T. Borgstrom, "Development and Characterization of a bottom-up InP Nanowire Solar Cell with 16.7% Efficiency," *Conference Record of the IEEE Photovoltaic Specialists Conference*, vol. 2020-June, pp. 1754–1756, 2020.

[67] P. Krogstrup, H. I. Jørgensen, M. Heiss, O. Demichel, J. V. Holm, M. Aagesen, J. Nygard, and A. Fontcuberta i Morral, "Single-nanowire solar cells beyond the Shockley–Queisser limit," *Nature Photonics*, vol. 7, no. March, pp. 1–5, 2013. arXiv: 1301.1068.

[68] N. Anttu, "Absorption of light in a single vertical nanowire and a nanowire array," *Nanotechnology*, vol. 30, no. 10, 2019.

[69] L. Wen, Z. Zhao, X. Li, Y. Shen, H. Guo, and Y. Wang, "Theoretical analysis and modeling of light trapping in high efficicency GaAs nanowire array solar cells," *Applied Physics Letters*, vol. 99, no. 14, 2011.

[70] O. L. Muskens, J. G. Rivas, R. E. Algra, E. P. Bakkers, and A. Lagendijk, "Design of light scattering in nanowire materials for photovoltaic applications," *Nano Letters*, vol. 8, no. 9, pp. 2638–2642, 2008.

[71] S. L. Diedenhofen, G. Vecchi, R. E. Algra, A. Hartsuiker, O. L. Muskens, G. Immink, E. P. Bakkers, W. L. Vos, and J. G. Rivas, "Broad-band and omnidirectional antireflection coatings based on semiconductor nanorods," *Advanced Materials*, vol. 21, no. 9, pp. 973–978, 2009.

[72] Z. Fan, R. Kapadia, P. W. Leu, X. Zhang, Y. L. Chueh, K. Takei, K. Yu, A. Jamshidi, A. A. Rathore, D. J. Ruebusch, M. Wu, and A. Javey, "Ordered arrays of dual-diameter nanopillars for maximized optical absorption," *Nano Letters*, vol. 10, no. 10, pp. 3823–3827, 2010.

[73] S. L. Diedenhofen, O. T. Janssen, G. Grzela, E. P. Bakkers, and J. Gómez Rivas, "Strong geometrical dependence of the absorption of light in arrays of semiconductor nanowires," *ACS Nano*, vol. 5, no. 3, pp. 2316–2323, 2011.

[74] G. Otnes and M. T. Borgström, "Towards high efficiency nanowire solar cells," *Nano Today*, pp. 1–15, 2016.

[75] N. Anttu, "Shockley-queisser detailed balance efficiency limit for nanowire solar cells," *ACS Photonics*, vol. 2, no. 3, pp. 446–453, 2015.

[76] K. Korzun, G. W. Castellanos, D. K. de Boer, J. Gómez Rivas, and J. E. Haverkort, "Nanowire Solar Cell Above the Radiative Limit," *Advanced Optical Materials*, vol. 9, no. 2, pp. 1–7, 2021.

[77] J. Matthews and A. Blakeslee, "Defects in epitaxial multilayers: I. misfit dislocations," *Journal of Crystal Growth*, vol. 27, pp. 118–125, 1974.

[78] S. A. Kalogirou, *McEvoy's Handbook of Photovoltaics - Fundamentals and Applications (3rd Edition)*. Elsevier, 2018.

[79] G. E. Cirlin, V. G. Dubrovskii, I. P. Soshnikov, N. V. Sibirev, Y. B. Samsonenko, A. D. Bouravleuv, J. C. Harmand, and F. Glas, "Critical diameters and temperature domains for MBE growth of III-V nanowires on lattice mismatched substrates," *Physica Status Solidi - Rapid Research Letters*, vol. 3, no. 4, pp. 112–114, 2009.

[80] A. Biermanns, S. Breuer, A. Trampert, A. Davydok, L. Geelhaar, and U. Pietsch, "Strain accommodation in Ga-assisted GaAs nanowires grown on silicon (111)," *Nanotechnology*, vol. 23, no. 30, 2012.

[81] M. T. Borgström, J. Wallentin, M. Heurlin, S. Fält, P. Wickert, J. Leene, M. H. Magnusson, K. Deppert, and L. Samuelson, "Nanowires with promise for photovoltaics," *IEEE Journal on Selected Topics in Quantum Electronics*, vol. 17, no. 4, pp. 1050–1061, 2011.

[82] J. V. Holm, H. I. Jørgensen, P. Krogstrup, J. Nygård, H. Liu, and M. Aagesen, "Surface-passivated GaAsP single-nanowire solar cells exceeding 10% efficiency grown on silicon," *Nature Communications*, vol. 4, pp. 1–5, 2013.

[83] M. Yao, S. Cong, S. Arab, N. Huang, M. L. Povinelli, S. B. Cronin, P. D. Dapkus, and C. Zhou, "Tandem Solar Cells Using GaAs Nanowires on Si: Design, Fabrication, and Observation of Voltage Addition," *Nano Letters*, vol. 15, no. 11, pp. 7217–7224,

[84] G. Mariani, A. C. Scofield, C.-H. Hung, and D. L. Huffaker, "GaAs nanopillar-array solar cells employing in situ surface passivation," *Nature communications*, vol. 4, p. 1497, 2013.

[85] Y. Cui, J. Wang, S. R. Plissard, A. Cavalli, T. T. T. Vu, R. P. J. van Veldhoven, L. Gao, M. Trainor, M. A. Verheijen, J. E. M. Haverkort, and E. P. A. M. Bakkers, "Efficiency enhancement of InP nanowire solar cells by surface cleaning.," *Nano letters*, vol. 13, no. 9, pp. 4113–7, Sep. 2013.

[86] Z. Zhong, Z. Li, Q. Gao, Z. Li, K. Peng, L. Li, S. Mokkapati, K. Vora, J. Wu, G. Zhang, Z. Wang, L. Fu, H. H. Tan, and C. Jagadish, "Efficiency enhancement of axial junction InP single nanowire solar cells by dielectric coating," *Nano Energy*, vol. 28, pp. 106–114, 2016.

[87] Y. Zhang and H. Liu, "Self-catalyzed GaAs(P) nanowires and their application for solar cells," *Journal of Physics D: Applied Physics*, vol. 53, no. 23, 2020.

[88] M. A. Green, E. D. Dunlop, J. Hohl-Ebinger, M. Yoshita, N. Kopidakis, and X. Hao, "Solar cell efficiency tables (Version 58)," *Progress in Photovoltaics: Research and Applications*, vol. 29, no. 7, pp. 657–667, 2021.

[89] C. Colombo, M. Heiß, M. Grätzel, and A. Fontcuberta I Morral, "Gallium arsenide p-i-n radial structures for photovoltaic applications," *Applied Physics Letters*, vol. 94, no. 17, 2009.

[90] B. Tian, X. Zheng, T. J. Kempa, Y. Fang, N. Yu, G. Yu, J. Huang, and C. M. Lieber, "Coaxial silicon nanowires as solar cells and nanoelectronic power sources," *Nature*, vol. 449, no. October, pp. 885–889, 2007.

[91] C. Gutsche, R. Niepelt, M. Gnauck, A. Lysov, W. Prost, C. Ronning, and F. J. Tegude, "Direct determination of minority carrier diffusion lengths at axial GaAs nanowire p-n junctions," *Nano Letters*, vol. 12, no. 3, pp. 1453–1458, 2012.

[92] M. Heiss and A. Fontcuberta I Morral, "Fundamental limits in the external quantum efficiency of single nanowire solar cells," *Applied Physics Letters*, vol. 99, no. 26, pp. 97–100, 2011.

[93] A. Nowzari, M. Heurlin, V. Jain, K. Storm, A. Hosseinnia, N. Anttu, M. T. Borgström, H. Pettersson, and L. Samuelson, "A comparative study of absorption in vertically and laterally oriented InP core-shell nanowire photovoltaic devices," *Nano Letters*, vol. 15, no. 3, pp. 1809–1814, 2015.

[94] W. S. Ko, T. T. D. Tran, I. Bhattacharya, K. W. Ng, H. Sun, and C. Chanhasnain, "Illumination Angle Insensitive Single Indium Phosphide Tapered Nanopillar Solar Cell," *Nano Letters*, vol. 15, no. 8, pp. 4961–4967, 2015.

[95] V. Piazza, M. Vettori, A. A. Ahmed, P. Lavenus, F. Bayle, N. Chauvin, F. H. Julien, P. Regreny, G. Patriarche, A. Fave, M. Gendry, and M. Tchernycheva, "Nanoscale investigation of a radial p-n junction in self-catalyzed GaAs nanowires grown on Si (111)," *Nanoscale*, vol. 10, no. 43, pp. 20 207–20 217, 2018.

[96] G. Otnes, E. Barrigo, C. Sundvall, K. E. Svensson, M. Heurlin, G. Siefer, L. Samuelson, I. Åberg, and M. T. Borgstro, "Understanding InP Nanowire Array Solar Cell Performance by Nanoprobe-Enabled Single Nanowire Measurements," *Nano Letters*, vol. 18, no. 5, pp. 3038–3046, 2018.

[97] E. Barrigón, L. Hrachowina, and M. T. Borgström, "Light current-voltage measurements of single, as-grown, nanowire solar cells standing vertically on a substrate," *Nano Energy*, vol. 78, no. May, 2020.

[98] C. Pan, S. Niu, Y. Ding, L. Dong, R. Yu, Y. Liu, G. Zhu, and Z. L. Wang, "Enhanced Cu 2S/CdS coaxial nanowire solar cells by piezo-phototronic effect," *Nano Letters*, vol. 12, no. 6, pp. 3302–3307, 2012.

[99] L. Zhu, L. Wang, C. Pan, L. Chen, F. Xue, B. Chen, L. Yang, L. Su, and Z. L. Wang, "Enhancing the Efficiency of Silicon-Based Solar Cells by the Piezo-Phototronic Effect," *ACS Nano*, vol. 11, no. 2, pp. 1894–1900, 2017.

[100] P. A. Alekseev, V. A. Sharov, B. R. Borodin, M. S. Dunaevskiy, R. R. Reznik, and G. E. Cirlin, "Effect of the uniaxial compression on the GaAs nanowire solar cell," *Micromachines*, vol. 11, no. 6, pp. 1–13, 2020.

[101] H. Hasegawa, "Fermi level pinning and schottky barrier height control at metal-semiconductor interfaces of InP and related materials," *Japanese Journal of Applied Physics, Part 1: Regular Papers and Short Notes and Review Papers*, vol. 38, no. 2 B, pp. 1098–1102, 1999.

[102] L. Hüttenhofer, D. Xydias, R. B. Lewis, S. Rauwerdink, A. Tahraoui, H. Küpers, L. Geelhaar, O. Marquardt, and S. Ludwig, "Optimization of Ohmic Contacts to n-Type GaAs Nanowires," *Physical Review Applied*, vol. 10, no. 3, p. 034 024, 2018.

[103] V. Rideout, "A review of the theory and technology for ohmic contacts to group III–V compound semiconductors," *Solid-State Electronics*, vol. 18, no. 6, pp. 541–550, 1975.

[104] Z. Zhang, K. Yao, Y. Liu, C. Jin, X. Liang, Q. Chen, and L. M. Peng, "Quantitative analysis of current-voltage characteristics of semiconducting nanowires: Decoupling of contact effects," *Advanced Functional Materials*, vol. 17, no. 14, pp. 2478–2489, 2007.

[105] F. A. Padovani and R. Stratton, "Field and thermionic-field emission in Schottky barriers," *Solid State Electronics*, vol. 9, no. 7, pp. 695–707, 1966.

[106] P. Chattopadhyay, "The effect of shunt resistance on the electrical characteristics of Schottky barrier diodes," *Journal of Physics D: Applied Physics*, vol. 29, no. 3, pp. 823–829, 1996.

[107] J. I. Goldstein, D. E. Newbury, J. R. Michael, N. W. Ritchie, J. H. J. Scott, and D. C. Joy, *Scanning Electron Microscopy and X-Ray Microanalysis*. Springer Science + Business Media New York, 2003.

[108] L. Reimer, *Scanning Electron Microscopy*. Springer-Verlag Berlin Heidelberg, 1998.

[109] H. Kazumori, K. Honda, M. Matsuya, M. Date, and C. Nielsen, "Field emission SEM with a spherical and chromatic aberration corrector," *Microscopy and Microanalysis*, vol. 10, no. SUPPL. 2, pp. 1370–1371, 2004.

[110] D. B. Williams and C. B. Carter, *Transmission Electron Microscopy: A Textbook for Materials Science*. Springer Science + Business Media, 2009.

[111] L. A. Gianuzzi and F. A. Stevie, *Introduction to Focused Ion Beams*. Springer Science + Business Media, Inc., 2005.

[112] A. Casadei, P. Krogstrup, M. Heiss, J. A. Röhr, C. Colombo, T. Ruelle, S. Upadhyay, C. B. Sørensen, J. Nygård, and A. Fontcuberta I Morral, "Doping incorporation paths in catalyst-free Be-doped GaAs nanowires," *Applied Physics Letters*, vol. 102, no. 1, 2013. arXiv: `arXiv:1210.1670v1`.

[113] P. Lavenus, A. Messanvi, L. Rigutti, A. De Luna Bugallo, H. Zhang, F. Bayle, F. H. Julien, J. Eymery, C. Durand, and M. Tchernycheva, "Experimental and theoretical analysis of transport properties of core-shell wire light emitting diodes probed by electron beam induced current microscopy," *Nanotechnology*, vol. 25, no. 25, 2014.